Research Square

Preprints are preliminary reports that have not undergone peer review.
They should not be considered conclusive, used to inform clinical practice,
or referenced by the media as validated information.

Viperin deficiency in CD4⁺ T cells enhances protective immunity against Mycobacterium tuberculosis infection

Xinying Zhou
Southern Medical University
Yun Liang
Southern Medical University
Lingming Lin
Southern Medical University
Hongxuan Li
Southern Medical University
Huilan Niu
Southern Medical University
Zhenyu Han
Southern Medical University
Minna Xu
Southern Medical University
Qian Wen
Southern Medical University
Liang Zhou
Southern Medical University
Chaoying Zhou
Southern Medical University
Li Ma
mali_61648322@smu.edu.cn
Southern Medical University

Research Article

Keywords: Viperin, Mycobacterium tuberculosis (Mtb), Tuberculosis, CD4+ T cell responses

Posted Date: November 9th, 2026

DOI: https://doi.org/10.21203/rs.3.rs-11479563/v1

License: This work is licensed under a Creative Commons Attribution 4.0 International License.
Read Full License

Additional Declarations: No competing interests reported.

Viperin deficiency in CD4$^+$ T cells enhances protective immunity against *Mycobacterium tuberculosis* infection

Xinying Zhou[a,b,c#*], Yun Liang[a,b,c#], Lingming Lin[a,b,c#], Hongxuan Li[a,b,c#], Huilan Niu[a,b,c], Zhenyu Han[a,b,c], Minna Xu[a,b,c], Qian Wen[a,b,c], Liang Zhou[a,b,c], Chaoying Zhou[a,b,c], Li Ma[a,b,c*]

[a]Institute of Molecular Immunology, School of Laboratory Medicine and Biotechnology, Southern Medical University, Guangzhou 510515, China.

[b]Key Laboratory of Infectious Diseases Research in South China, Ministry of Education, Southern Medical University, Guangzhou 510515, China.

[c]State Key Laboratory of Multi-organ Injury Prevention and Treatment, Southern Medical University, Guangzhou 510515, China

Short Title: Viperin deficiency in CD4$^+$ T cells inhibits Mtb survival

# These authors contributed equally to this work.

*Corresponding author:

Dr. Li Ma

Li Ma, PhD, Institute of Molecular Immunology, School of Laboratory Medicine and Biotechnology, Southern Medical University, Guangzhou 510515, China. Phone: +86-20-61648322, Fax: +86-20-61648322. E-mail: mali_61648322@smu.edu.cn

Dr. Xinying Zhou

Xinying Zhou, PhD, Institute of Molecular Immunology, School of Laboratory Medicine and Biotechnology, Southern Medical University, Guangzhou 510515, China. Phone: +86-20-61648553, Fax: +86-20- 61648555. E-mail: zxyforever@smu.edu.cn

Number of Figures: 7

Word count: 9909 (Including abstract and body text, references, figures and tables).

Keywords: Viperin, *Mycobacterium tuberculosis* (Mtb), Tuberculosis, CD4$^+$ T cell responses.

Abstract

Tuberculosis (TB), caused by *Mycobacterium tuberculosis* (Mtb), remains a major global health threat. $CD4^+$ T cells are indispensable for protective immunity against Mtb infection. This study defines the T-cell-intrinsic role of Viperin (encoded by *Rsad2*) during Mtb infection. We utilized T cell-specific Viperin knockout ($Rsad2^{cko}$) mice and adoptive transfer models into $Rag1^{-/-}$ hosts to assess outcomes following aerosol Mtb infection. We found that Viperin deficiency in $CD4^+$ T cells significantly reduced bacterial burden and pathology in Mtb-infected lungs. This enhanced protection was associated with an increased frequency and activation of Mtb-specific $CD4^+$ T cells. Viperin-deficient $CD4^+$ T cells exhibited enhanced early activation, proliferation, and a bias towards differentiating into short-lived effector memory (Tem) over central memory (Tcm) cells. Furthermore, these cells showed a pronounced skewing towards a Th1 phenotype, with robust IFN-γ production, both *in vivo* and under Th1-polarizing conditions *in vitro*. Viperin-deficient $CD4^+$ T cells displayed reduced apoptosis and increased activation of the PI3K-Akt-mTOR and PKC-θ-NF-κB pro-survival pathways upon T cell receptor (TCR) stimulation, accompanied by transcriptional downregulation of the pro-apoptotic mediator Bbc3 (PUMA) and the proliferation brake Gadd45a *in vivo*. Collectively, our study reveals that Viperin intrinsically dampens $CD4^+$ T cell function by restraining Th1 differentiation, proliferation, and survival, thereby identifying Viperin as a potential immunotherapeutic target for enhancing T cell-mediated defense against TB. These findings also highlight a context-dependent duality of Viperin, which is protective in viral infection but detrimental in Mtb infection, underscoring its role as a homeostatic regulator of T cell immunity.

Introduction

Tuberculosis (TB), caused by *Mycobacterium tuberculosis* (Mtb), remains the leading cause of death from a single infectious agent worldwide, representing an urgent global public health crisis [1, 2]. Following exposure, only an estimated 5-10% of immunocompetent individuals progress to active TB disease; the majority establish a latent infection (LTBI), wherein the host immune system successfully contains but does not eradicate the bacilli [1]. The critical determinant of this outcome is the host immune response, with $CD4^+$ T cells playing an indispensable role in protective immunity. Upon Mtb infection, antigen presentation leads to the activation and differentiation of $CD4^+$ T cells, which are central to orchestrating the cellular immune response necessary for granuloma formation and bacterial control [3, 4]. Therefore, elucidating the molecular mechanisms that regulate $CD4^+$ T cell function is paramount for identifying novel therapeutic strategies against TB.

Viperin (encoded by *Rsad2* gene) is an interferon-stimulated protein renowned for its broad-spectrum antiviral activity and emerging roles in immunometabolic regulation [5]. While Viperin is well established as a host defense factor that amplifies type I IFN signaling and promotes $CD8^+$ T cell effector function during viral infection, its role in bacterial immunity appears to be fundamentally different. Our previous work has demonstrated that Viperin acts as a negative regulator of innate immunity against Mtb. In macrophages, Viperin impairs innate immune signaling and interferon-gamma production [6, 7]. In dendritic cells, it suppresses inflammatory responses, antigen presentation, and the subsequent priming of $CD4^+$ and $CD8^+$ T cells [8]. These findings establish Viperin as a significant immunosuppressive factor within the innate immune compartment during Mtb infection. However, the immune defense against Mtb is a continuum involving both innate and adaptive arms. While the inhibitory role of Viperin in antigen-presenting cells is evident, its potential function within the adaptive immune system, specifically in the critical $CD4^+$ T cell

population, remains completely unknown. It is unclear whether Viperin is expressed in T cells and whether it intrinsically regulates their differentiation, proliferation, or effector functions during the anti-mycobacterial response. Furthermore, given the apparent contradiction between Viperin's antiviral and antimycobacterial functions, it remains to be determined whether Viperin regulates $CD4^+$ T cell responses through a common mechanism that is differentially deployed depending on the pathogen context.

In this study, we hypothesized that Viperin functions as a T-cell-intrinsic negative regulator to constrain $CD4^+$ T cell-mediated immunity against Mtb. To investigate whether Viperin regulates $CD4^+$ T function to influence Mtb survival, we employed T cell-specific *Rsad2* conditional knockout mice (CD4-Cre/*Rsad2*$^{flox/flox}$, *Rsad2*^{cko}) mice and adoptive transfer models into *Rag1*-deficient hosts (*Rag1*$^{-/-}$ mice). We report that targeted deletion of Viperin in $CD4^+$ T cells significantly enhances host resistance to Mtb infection. This protective effect is associated with augmented activation, expansion, and effector function of lung $CD4^+$ T cells. Our findings reveal a novel mechanism of immune regulation in TB, identifying Viperin as a potential host-directed therapeutic target to enhance T-cell-mediated protection.

Materials and Methods

Ethics statement

This study adhered to ICMJE guidelines and approved by the Ethics Committee of Southern Medical University. All animal experiments were performed following the Guide for the Care and Use of Laboratory Animals published by the U.S. National Institutes of Health (NIH). Moreover, all experimental protocols were reviewed and approved by both the Medical Ethics Committee and the Biosafety Management Committee of Southern Medical University. The letter of commitment for the management of laboratories handling highly pathogenic microorganisms was also approved by Southern Medical University.

Laboratory mice

C57BL/6J mice were purchased from the Laboratory Animal Center of Southern Medical University (Guangzhou, China). T cell-specific *Rsad2* conditional knockout mice (CD4-Cre/*Rsad2*$^{flox/flox}$, *Rsad2*^{cko}) mice and control mice (CD4-flox/*Rsad2*$^{flox/flox}$, *Rsad2*^{flox}) mice on a C57BL/6J background were generated by Cyagen Biosciences Inc. (Cat. No.: KOCMP-02845-Rsad2, Nanjing, China). *Rag* gene-deficient (*Rag*$^{-/-}$) mice and CD45.1 congenic mice, both on a C57BL/6J background, were obtained from GemPharmatech Co., Ltd. (Jiangsu, China). All mice were housed in the Laboratory Animal Center of Southern Medical University under specific pathogen-free (SPF) conditions.

Culture and infection of Mtb

Mtb H37Rv strain (American Type Culture Collection, Cat. No. 7294) was inoculated into 7H9 liquid medium (Becton Dickinson, New Jersey, USA) supplemented with 10% OADC [containing 0.06% (v/v) oleic acid (Sigma, St. Louis, Missouri, USA), 5% albumin (Sigma, St. Louis, Missouri, USA), 100 mM glucose (GHTECH, Guangzhou, China), 0.003% catalase (Sigma, St. Louis, Missouri, USA), and 145 mM sodium chloride (GHTECH, Guangzhou, China)]. The culture was incubated at 37 °C in a 5% CO_2 incubator. Subculture was performed monthly to maintain the activity and virulence

of the strain. A single bacterial suspension was prepared by gentle vortexing and filtration through a 5-μm filter for infection experiments. The concentration of the single bacterial suspension was determined by measuring the absorbance at a wavelength of 600 nm (OD_{600}) using a microplate reader (Thermo Fisher Scientific, Carlsbad, California, USA). The suspension was then diluted in sterile PBS to a total of 1×10^6 Mtb in a final volume of 3 mL and loaded into the nebulizer. Mice were infected with H37Rv using an inhalation exposure system (Glas-Col, USA). For each infection batch, six mice were placed in the circular aerosol chamber and exposed simultaneously for 30 min. To confirm the uniformity and calibrate the delivery efficiency of our infection model, the baseline bacterial burden was evaluated in a separate cohort of mice (**Supplementary Fig.1**). Under our standardized preparation protocol, the implanted dose was approximately 10,000 CFU per mouse at Day 1 post-infection. This confirmed that all mice in the experimental cohorts received a consistent and viable initial Mtb burden, and the 4-week and 6-week bacterial burdens were subsequently evaluated by plating serial dilutions.

Adoptive T Cell Transfer Assay

Naive $CD4^+$ T cells were isolated from the spleens of CD45.1 mice and *Rsad2*^{cko} mice using a Mouse Naive $CD4^+$ T Cell Isolation Kit (Miltenyi Biotec, Germany). The purity of the isolated cells was determined by flow cytometry, with the requirement that purity ≥ 95%. One week prior to *Mycobacterium tuberculosis* infection, each *Rag1*$^{-/-}$ mouse was intravenously injected with 2×10^6 cells via the tail vein, and no additional special treatments were performed on the recipient mice.

Colony-Forming Unit (CFU) Assay

Mice were euthanized, and lungs and spleens were harvested at week 4 and week 6 post-infection. The mouse lung/spleen tissues were lysed in double-distilled water (ddH_2O) containing 0.1% Triton X-100 (Solarbio Science & Technology Co., Ltd., Beijing, China). Following homogenization, the lysates were serially diluted in 0.1% Triton X-100 with thorough mixing at each step. Lung tissue samples were diluted to

final concentrations of 1:2000, 1:4000, and 1:10,000, while spleen tissue samples were diluted 1:2000. A 50 µL aliquot of the diluted suspension was pipetted onto 7H10 agar plates (Becton Dickinson and Company, New Jersey, USA), and the bacterial suspension was evenly spread across the agar surface using a sterile spreader. Each group was set up with 6-10 biological replicates. After spreading, the 7H10 agar plates were sealed with Parafilm M sealing film (Bemis Company, USA), inverted, and incubated at 37 °C in a humidified incubator with 5% CO_2. Following 20-30 days of incubation, CFUs were counted against a black background.

Hematoxylin-Eosin (HE) Staining and Immunohistochemical (IHC) Analysis

Female C57BL/6J mice aged 4-6 weeks with similar body weights, including *Rsad2*^{flox} and *Rsad2*^{cko} mice, were selected. Mice were infected with Mtb H37Rv strain via an inhalation exposure system (Glas-Col, USA) at an infectious dose of 1×10^6 CFUs per mouse. At 6 weeks post-infection, the mice were euthanized and aseptically dissected. Lung tissues were isolated and immediately fixed in 4% paraformaldehyde solution (Leagene Biotechnology Co., Ltd., Beijing, China) for 24 hrs. The fixed tissues were dehydrated in a graded series of anhydrous ethanol (Sinopharm Group Co., Ltd., Beijing, China), cleared in xylene (Sinopharm Group Co., Ltd., Beijing, China), and embedded in paraffin after immersion in molten wax at 60 °C for 2 hrs. Serial 5 µm-thick sections were cut and mounted onto poly-L-lysine-coated glass slides, followed by baking at 60 °C for 2 hrs for subsequent use. For HE staining, the paraffin sections were subjected to routine dewaxing and rehydration, and the staining procedure was performed by Pinuofei Biotechnology Co., Ltd. Briefly, sections were stained with hematoxylin for 5 min, differentiated in acidified ethanol for 30 seconds, and counterstained with eosin for 2 min. After dehydration and clearing, the sections were mounted with neutral balsam. Inflammatory infiltration and pathological damage in lung tissues were observed and photographed under a light microscope. For quantitative analysis of HE staining, images were analyzed using Fiji software (ImageJ). Physical length was first calibrated using the scale bar embedded in each

image (Set Scale function). Target regions were defined using the direct Color Threshold method in the HSB color space. To ensure data consistency, uniform and fixed threshold parameters were applied to all images: the upper Brightness limit for the total lung tissue area was set to 250 to exclude blank slide backgrounds, and the upper Brightness limit for the inflammatory infiltrate was set to 0-160 to precisely extract the densely stained and nuclei-rich inflammatory regions. Following binarization (Make Binary), the inflammatory area and the total lung tissue area were measured within the entire field of view. The percentage of the inflammatory area was finally calculated as: Inflammatory area (%) = (inflammatory area/total lung tissue area) × 100%.

For IHC staining, dewaxed and rehydrated paraffin sections were processed by Pinuofei Biotechnology Co., Ltd. Antigen retrieval was performed by microwave heating in citrate buffer (pH 6.0) for 15 min, followed by natural cooling to room temperature. Endogenous peroxidase activity was blocked by incubating the sections with 3% hydrogen peroxide solution at room temperature for 10 min, followed by three washes with phosphate-buffered saline (PBS). The sections were then blocked with goat serum blocking buffer at 37 °C for 30 min. After removing the blocking buffer, primary antibody against CD4 (diluted at 1:200) was added, and the sections were incubated overnight at 4 °C. On the next day, the sections were rewarmed at room temperature for 30 min and washed three times with PBS. Horseradish peroxidase (HRP)-conjugated secondary antibody (diluted at 1:500) was applied, and the sections were incubated at 37 °C for 1 hour, followed by three PBS washes. Color development was performed using 3, 3’-diaminobenzidine (DAB) chromogen in the dark for 3–5 min, and the cell nuclei were counterstained with hematoxylin. After dehydration and clearing, the sections were mounted with neutral balsam. $CD4^+$ positive cells (stained brownish-yellow) were observed and photographed under a light microscope. The integrated optical density per unit area (IOD/Area) was calculated using Image J software, with 5 non-overlapping fields randomly selected

per sample for mean value calculation.

Flow Cytometry (FCM) Analysis

For flow cytometric analysis, target cells were first collected and fixed with Fixation Buffer (BioLegend, USA) for 20 min. After washing with IRS-PBS (1× phosphate-buffered saline (PBS) containing 1% bovine serum albumin (BSA, Sigma, St. Louis, MO, USA)), the cells were incubated with fluorochrome-conjugated monoclonal antibodies (mAbs) or isotype control antibodies on ice in the dark for 30 min to stain cell surface markers. For intracellular targets, the fixed cells were subsequently permeabilized using Intracellular Staining Perm Wash Buffer (10×) (BioLegend, USA) diluted with double-distilled water (ddH_2O). Following incubation and two rounds of washing (centrifuged at 350 g for 5–10 min), the corresponding mouse monoclonal antibodies were added and incubated in the dark for 1 hour to detect intracellular cytokines. For nuclear targets (such as transcription factors), a separate aliquot of fixed cells was permeabilized using a working concentration of Fixation/Permeabilization buffer prepared from the Concentrate and Diluent (eBioscience, USA) to achieve nuclear membrane permeabilization. The cells were then stained with antibodies against nuclear targets (prepared in the eBioscience permeabilization buffer) for 1 hour. All stained samples were acquired on a BD LSRFortessa flow cytometer. After gating on viable cells, the positive percentage and fluorescence intensity of target-labeled cells were recorded, and subsequent analyses were performed using FlowJo software (Tree Star). All gates were established based on isotype control antibodies to ensure consistent analysis across samples. The specific flow antibodies used in this study are detailed in **Supplementary Table 1**.

Detection of Antigen-Specific $CD4^+$ and $CD8^+$ T Cells by MHC Tetramer Staining

To detect Mtb-specific $CD4^+$ and $CD8^+$ T cells, single-cell suspensions were prepared from the lungs of Mtb-infected mice according to standard protocols. Briefly, tissues were collected and processed into single-cell suspensions, and cells were

resuspended at a concentration of 2 × 10^7 cells/mL. A 50 µL aliquot of the cell suspension (approximately 1 × 10^6 cells) was used per tetramer assay. For each 12 × 75 mm tube, 10 µL of Clear Back (human FcR blocking reagent) (MTG-001, MBL, Medical & Biological Laboratories Co., Ltd, Nagoya, Japan) was added, followed by the addition of 50 µL of cell suspension. The mixture was incubated at room temperature for 5 min.

For $CD4^+$ T cell tetramer staining, 10 µL of I-Ab ESAT-6_{1-20} Tetramer-PE (TS-M707-1, MBL, Medical & Biological Laboratories Co., Ltd, Nagoya, Japan) was added and gently vortexed. The samples were incubated at 2-8 °C in the dark for 30-60 min. Subsequently, additional anti-CD4 antibody were added as needed and gently vortexed, followed by further incubation at 2-8 °C in the dark for 30 min. For $CD8^+$ T cell tetramer staining, 10 µL of T-Select MHC class I mouse tetramer-APC (TS-M549-P, MBL, Medical & Biological Laboratories Co., Ltd, Nagoya, Japan) was added and gently vortexed. The samples were incubated at 2-8 °C in the dark for 30-60 min. Subsequently, additional anti-CD8 antibody were added as needed and gently vortexed, followed by further incubation at 2-8 °C in the dark for 30 min.

After incubation, 800 µL of FCM buffer (PBS containing 2% fetal bovine serum) was added to each tube, and the samples were centrifuged at 400 × g for 5 min. Red blood cells were then lysed. The cells were fixed with 200 µL of Fixation Buffer, washed by centrifugation, and the pellet was resuspended in 400 µL of IRS-PBS. The samples were stored at 4 °C in the dark until flow cytometric analysis. All stained samples were acquired on a BD LSRFortessa flow cytometer. The frequency of $tetramer^+$ cells was calculated as a percentage of total $CD4^+$ or $CD8^+$ T cells using FlowJo software. All tetramer gates were established using an isotype control or unloaded tetramer control to ensure consistent analysis across samples.

***In Vitro* Sorting and Culture of T Cells**

Female C57BL/6J mice aged 4-6 weeks with similar body weights, including *Rsad2*^{flox} and *Rsad2*^{cko} mice, were selected. Splenocytes were obtained by grinding the spleens

into homogenates. Naive $CD4^+$ T cells were isolated from the splenic homogenates using a Mouse Naive $CD4^+$ T Cell Isolation Kit (Miltenyi Biotec, Germany). The purity of the isolated cells was verified by flow cytometry to be ≥ 95%. For TCR stimulation and Th polarization, 96-well plates were pre-coated overnight at 4°C with 5 μg/mL anti-mouse CD3ε (TONBO, India) and 2 μg/mL anti-mouse CD28 (TONBO, India). On the following day, the unbound coating antibodies were removed by aspiration and washed thoroughly. The isolated naive $CD4^+$ T cells or total splenocytes were then resuspended in T cell medium containing the corresponding cytokines and seeded into the pre-coated 96-well plate. The cells were incubated at 37 °C with 5% CO_2 for 24, 48, and 72 hrs.

For basal TCR activation, naive $CD4^+$ T cells were activated with plate-bound anti-CD3 (5 μg/mL) and soluble anti-CD28 (2 μg/mL) in the presence of 10 ng/mL rmIL-2. For Th1 polarization, the medium was supplemented with 10 ng/mL rmIL-12 and 10 μg/mL anti-IL-4 (clone 11B11). For Th2 polarization, the medium was supplemented with 20 ng/mL rmIL-4 and 10 μg/mL anti-IFN-γ (clone XMG1.2).

RNA Extraction and Quantitative Real-time Polymerase Chain Reaction (qRT-PCR)

Total RNA was extracted from $CD4^+$ T cells isolated from mouse lung tissues using TRIzol reagent (Thermo Fisher Scientific, Carlsbad, California, USA). RNA concentration was measured with a Nanodrop 2000 spectrophotometer (Thermo Fisher Scientific, Carlsbad, California, USA), with the required A260/A280 ratio ranging from 1.8 to 2.0. cDNA synthesis and reverse transcription were performed using TransScript® II First-Strand cDNA Synthesis SuperMix (TransGen Biotech, China). Quantitative real-time PCR was carried out using the SYBR® Premix Ex Taq™ II (Tli RNaseH Plus) kit (Takara Bio Inc., Beijing, China; Cat. No. RR820A) on a LightCycler 480 Real-Time PCR System (Roche, Basel, Switzerland) to detect the mRNA expression levels of target genes. The qPCR reaction was run with a three-step protocol: pre-denaturation at 95 °C for 2 min; 40 cycles of denaturation at 95 °C for 15 s, annealing at 60 °C for 15 s, and extension at 68 °C for 20 s; and final storage at

4 °C. Three technical replicates were set up for each sample, and a no-template control (NTC) was included simultaneously to eliminate contamination interference. The expression levels of all PCR products were normalized against the transcripts of glyceraldehyde-3-phosphate dehydrogenase (GAPDH) or β-actin as reference genes. The relative expression levels of target genes were calculated using the $2^{-\Delta\Delta CT}$ method and expressed as fold change relative to the control group. The complete primer sequences of target genes and reference genes used in the experiment are provided in **Supplementary Table 2**.

Western Blot Analysis

Cells were washed three times with 1 × PBS buffer, followed by the addition of protein lysis buffer [consisting of 455 mM Tris-HCl (pH 6.8, Sangon Biotech Co., Ltd., Shanghai, China), 41.6 mM sodium dodecyl sulfate (SDS, Zhuosheng Biotechnology Co., Ltd., Shanghai, China), 26.9 μM bromophenol blue (Solarbio Science & Technology Co., Ltd., Beijing, China), 30% (v/v) glycerol (Sigma, St. Louis, Missouri, USA), 10 μM dithiothreitol (DTT, Sigma, St. Louis, Missouri, USA), protease inhibitor cocktail (Neoscience Biotech Co., Ltd., China), and phosphatase inhibitor cocktail (Neoscience Biotech Co., Ltd., China)]. The samples were heated in a metal dry bath at 95 °C for 10 min to achieve complete protein denaturation.

SDS-PAGE electrophoresis was performed with a separating gel concentration of 8%–15%. Proteins were transferred onto a methanol (Guanghua Technology Co., Ltd., Guangdong, China)-activated PVDF membrane (Merck, Germany). The membrane was blocked with 5% BSA in PBST at room temperature for 1 hour, then incubated with the primary antibody at 4 °C overnight. After three washes with PBST, the membrane was incubated with horseradish peroxidase (HRP)-conjugated goat anti-rabbit or goat anti-mouse secondary antibody (Cell Signaling Technology, Danvers, Massachusetts, USA) at room temperature for 1 hour. Following another three washes with PBST, the target protein bands were visualized using an enhanced chemiluminescence (ECL) kit (Neoscience Biotech Co., Ltd., China) on a FluorChem

imaging system (ProteinSimple, USA). Quantitative densitometry values of all Western blot bands were obtained via scanning with Image J software (National Institutes of Health, USA). β-actin was used as the internal reference to calculate the relative expression level of target proteins (ratio of phosphorylated protein to total protein). Detailed information on all antibodies used in the experiment is provided in **Supplementary Table 3**.

RNA Sequencing (RNA-seq) Analysis

Naive $CD4^+$ T cells were isolated from the spleens of *Rsad2*^{flox} and *Rsad2*^{cko} C57BL/6J mice using a Mouse Naive $CD4^+$ T Cell Isolation Kit (Miltenyi Biotec, Germany). $CD4^+$ T cells from mouse spleens stimulated with TCR for 24 h were selected for subsequent experiments. Total RNA was extracted from mouse splenic $CD4^+$ T cells using TRIzol reagent (Thermo Fisher Scientific, Carlsbad, California, USA). RNA concentration was measured with a Nanodrop 2000 spectrophotometer (Thermo Fisher Scientific, Carlsbad, California, USA), with the A260/A280 ratio required to be between 1.8 and 2.0. The subsequent library construction and sequencing procedures were entrusted to GenoCare Bioinformatics Technology Co., Ltd. Messenger RNA (mRNA) was enriched using Oligo (dT) magnetic beads to construct cDNA sequencing libraries, and paired-end sequencing (PE150) was performed on the Illumina NovaSeq 6000 platform. The sequencing data volume of each sample was ≥ 6 Gb to ensure that the sequencing depth met the requirements for differential gene detection. Raw data were filtered to obtain clean reads, which were then aligned to the mouse reference genome (GRCm39) for gene expression quantification (expressed as FPKM values). Differential genes were screened using DESeq2 software with the criteria of |log2 fold change (log2FC)| ≥ 1 and adjusted P-value (padj) < 0.05. Gene Ontology (GO) functional annotation and Kyoto Encyclopedia of Genes and Genomes (KEGG) pathway enrichment analysis were performed on the differential genes. Principal component analysis (PCA) and differential gene heatmaps were used to visually display the sample clustering differences.

$CD4^+$ T Cell Cycle Assay

Cell cycle was detected using the Cell Cycle and Apoptosis Analysis Kit (Yeasen Biotechnology Co., Ltd., China). Cells in 96-well plates were pipetted to form a homogeneous suspension and collected into 1.5 mL Eppendorf (EP) tubes. The cells were pelleted by centrifugation at 800 × g for 5 min at 4 °C, and the supernatant was carefully aspirated. Then, 1 mL of pre-chilled PBS was added to resuspend the cells, followed by another centrifugation at 800 × g for 5 min at 4 °C to collect the cell pellet. The cell pellet was gently mixed with 1 mL of pre-chilled 70% ethanol and fixed at 4 °C for more than 2 hrs or overnight (Permeabilization Buffer can be used as an alternative). After fixation, the cells were pelleted by centrifugation at 1000 × g for 5 min at 4 °C, resuspended in 1 mL of pre-chilled PBS, and centrifuged again at 1000 × g for 5 min at 4 °C to harvest the cell pellet. Propidium iodide (PI) staining solution was prepared by mixing 0.5 mL of staining buffer, 10 µL of PI stock solution, and 10 µL of RNase A, and the mixture was set aside for use. Then, 0.5 mL of the above staining solution was added to each tube to gently resuspend the cells. The cells were incubated at room temperature in the dark for 30 min. The binding of PI to cellular DNA was detected by flow cytometry to analyze the cell cycle.

$CD4^+$ T Cell Proliferation Assay

Cell proliferation was detected using the CFDA SE Cell Proliferation and Tracking Assay Kit (Yeasen Biotechnology Co., Ltd., China). Cells were harvested by centrifugation and resuspended in 1 mL of 1 × cell staining buffer in a 15 mL centrifuge tube, with the cell concentration adjusted to 1×10^6 cells/mL. CFDA SE working solution was added to a final concentration of 5 µg/mL. After gentle mixing, the cells were incubated for 10 min in a constant-temperature CO_2 incubator at 37 °C. Immediately, approximately 10 mL of complete cell culture medium was added to the 15 mL centrifuge tube, and the mixture was inverted several times at room temperature to terminate the labeling reaction. The cells were centrifuged at 800 × g for 5 min at room temperature, the supernatant was discarded, and the cell pellet

was washed once by centrifugation with 5 mL of complete cell culture medium. The pellet was then resuspended in 5 mL of T cell culture medium and incubated for 10 min in a constant-temperature CO_2 incubator at 37 °C. Approximately 10 mL of complete cell culture medium was added to terminate the labeling reaction again, followed by centrifugation at 800 × g for 5 min at room temperature and supernatant discarding to complete the final wash. The cell pellet was resuspended in T cell culture medium and seeded in a 96-well plate for 72 hrs of culture. Subsequently, CFSE fluorescence intensity was detected by flow cytometry to analyze the cell proliferation index.

$CD4^+$ T Cell Apoptosis Assay

Cell apoptosis was detected using the Annexin V-FITC/PI Cell Apoptosis Detection Kit (Yeasen Biotechnology Co., Ltd., China). Cells were harvested by centrifugation and washed twice with pre-chilled PBS, with centrifugation at 300 × g for 5 min at 4 °C per wash. The PBS was discarded, and the cells were resuspended in 100 µL of 1 × Binding Buffer. Then 5 µL of Annexin V-FITC and 10 µL of PI Staining Solution were added, and the mixture was gently mixed and incubated for 10–15 min at room temperature in the dark. After adding 400 µL of 1× Binding Buffer and mixing well, the sample was placed on ice. Apoptosis was detected by flow cytometry within 1 hour.

Enzyme-Linked Immunosorbent Assay (ELISA)

The assay was performed using an ELISA kit (Abclonal, Wuhan, China). First, the standard was serially diluted two-fold, with sample diluent serving as the blank control, to generate an 8-point standard curve. The required microplate strips were detached from the frame, and 100 µL of the standard, diluted samples, or blank control was added to each well. After mixing thoroughly, the plate was sealed and incubated at 37 °C for 2 hrs. The liquid in the wells was discarded, and each well was washed three times with 200 µL of washing buffer using a Model 50TS Microplate Washer (Biotek, USA). Then, 100 µL of biotinylated antibody working solution was

added to each well; the plate was sealed and incubated at 37 °C for 1 h, followed by three washes and patting dry. Subsequently, 100 µL of streptavidin-HRP working solution was added to each well; the plate was sealed and incubated at 37 °C for 30 min, then washed three times and patted dry. Next, 100 µL of TMB substrate solution was added to each well and incubated at room temperature in the dark for 15 min. The reaction was immediately terminated by adding 50 µL of stop solution. The optical density (OD) values at 450 nm (with a reference wavelength of 570 nm) were measured using a microplate reader within 15 min. A standard curve was plotted using GraphPad Prism 10.0 software via four-parameter fitting (with $R^2 \geq 0.99$), and the sample concentrations were calculated and corrected for the dilution factor.

Statistical Analysis

All experimental data in this study were statistically analyzed using Prism 10.0 or SPSS 24.0 software. Measurement data were expressed as mean ± standard error of the mean (mean ± SEM). All detection indicators were verified by at least 3 independent replicate experiments to ensure the reliability of the results. Intergroup comparisons were performed using the independent-samples t-test, one-way analysis of variance (One-Way ANOVA), or two-way analysis of variance (Two-Way ANOVA) followed by Sidak's multiple-comparison test, as appropriate. Differences were considered statistically significant at $*p \leq 0.05$, $**p \leq 0.01$, $***p \leq 0.001$, and $****p \leq 0.0001$.

Results

CD4$^+$ T cell-intrinsic Viperin deficiency is sufficient to enhance host resistance to Mtb infection

To investigate the role of Viperin (*Rsad2*) in regulating CD4$^+$ T cells in the outcome of Mtb infected mice, we infected T cell-specific *Rsad2* conditional knockout mice (CD4-Cre/*Rsad2*$^{flox/flox}$, *Rsad2*^{cko}) mice and control mice (CD4-flox/*Rsad2*$^{flox/flox}$, *Rsad2*^{flox}) mice with 1×10^6 Mtb using aerosol inhalation method. Efficient deletion in CD4$^+$ T cells was confirmed by the almost complete loss of Viperin protein expression in splenic CD4$^+$ T cells from *Rsad2*^{cko} mice (**Fig. 1A**). The bacterial burden at Day 1 post-infection was comparable between *Rsad2*^{cko} and *Rsad2*^{flox} mice (**Supplementary Fig. 1**), confirming equivalent initial infection doses. *Rsad2*^{cko} mice exhibited significantly reduced bacterial loads in the lungs at 4- and 6-weeks post-infection (**Fig. 1B, C**). Histological analysis further revealed markedly alleviated pulmonary inflammation in *Rsad2*^{cko} mice, with a significantly lower inflammatory area percentage than that in *Rsad2*^{flox} mice (**Fig. 1D, E**). To directly assess the T-cell-intrinsic effect, we adoptively transferred naïve CD4$^+$ T cells from *Rsad2*^{cko} or control mice of *Rsad2*^{flox} into *Rag1*$^{-/-}$ recipient mice one week prior to Mtb infection. Recipients of *Rsad2*-deficient CD4$^+$ T cells showed significantly lower bacterial burdens in lungs and spleens at 4 weeks post-infection **(Fig. 1F-H)**. These results demonstrate that Viperin deficiency in CD4$^+$ T cells enhances host control of Mtb infection.

Viperin deficiency selectively promotes Mtb-specific CD4$^+$ T cell responses

Given the central role of CD4$^+$ T cells in anti-mycobacterial immunity, we analyzed T cell populations in infected mice. *Rsad2*^{cko} mice displayed a significantly higher proportion of CD4$^+$, but not CD8$^+$, T cells in lungs and spleens post-infection **(Fig. 2A-C)**. Furthermore, immunohistochemistry showed that CD4 expression was higher

in the lungs of *Rsad2*^{cko} mice than in control mice **(Fig. 2D)**. The frequency of ESAT-6_{1-20} tetramer$^+$ CD4$^+$ T cells was also increased in the lungs of Rsad2cko mice **(Fig. 2E)** indicating expansion of Mtb-specific cells. In contrast, the frequency of Mtb-specific tetramer$^+$ CD8$^+$ T cells showed no significant difference between *Rsad2*^{cko} and *Rsad2*^{flox} mice at 4 weeks post-infection **(Fig. 2F)**, consistent with the unchanged proportion of total CD8$^+$ T cells **(Fig. 2A-C)**. These results indicate that Viperin deficiency selectively enhances Mtb-specific CD4$^+$ T cell responses without affecting Mtb-specific CD8$^+$ T cell responses.

To directly test whether this enhancement was T-cell-intrinsic, we performed competitive adoptive transfer experiments into *Rag1*$^{-/-}$ hosts. *Rsad2*-deficient CD4$^+$ T cells (CD45.2$^+$) and control cells (CD45.1$^+$) were co-transferred at a 1:1 ratio, and *Rsad*2-deficient CD4$^+$ T cells outcompeted control cells in populating the host at 1, 2, and 4 weeks post-infection **(Fig. 2G-I)**. *In vitro*, upon TCR stimulation (anti-CD3/anti-CD28) without exogenous IL-2, a higher proportion of *Rsad2*^{cko} CD4$^+$ T cells persisted compared to controls, whereas the proportion of *Rsad2*^{cko} CD8$^+$ T cells was significantly reduced **(Fig. 2J-L)**. These data suggest that Viperin deficiency selectively promotes the accumulation and early activation of Mtb-specific CD4$^+$ T cells, without affecting Mtb-specific CD8$^+$ T cell responses.

Transcriptomic profiling reveals Viperin regulates multiple functional pathways in CD4$^+$ T cells

To investigate the molecular basis of Rsad2 function, we performed RNA-seq on *Rsad2*^{cko} and *Rsad2*^{flox} CD4$^+$ T cells 24 h post-TCR stimulation. PCA confirmed a clear separation between the two groups **(Fig. 3A)**, and volcano plot analysis identified 699 differentially expressed genes (DEGs) **(Fig. 3B)**. To identify the key drivers of this transcriptomic shift, we analyzed the 25 most differentially expressed genes. The heatmap revealed a profound downregulation of effector molecules (Gzma, Gzmb) and survival/proliferation regulators (Il7r, Cdk6) in *Rsad2*^{cko} cells **(Fig. 3C)**.

Consistently, GO enrichment analysis showed that these DEGs were predominantly enriched in RNA metabolism, ribosome biogenesis, and translational machinery **(Fig. 3D)**, suggesting a profound remodeling of the cellular translational program upon *Rsad2* deletion.

The heatmap for "cell activation involved in immune response" **(Fig. 3E)** revealed a profound upregulation of activation-associated genes (*Tfrc*, *Hspd1*, *Lgals3*, *Eomes*) alongside a marked downregulation of regulatory markers (*Cx3cr1*, *Il4*, *Gata3*, *Tnfaip3*). This hyperactivated profile was accompanied by a dysregulated proliferation signature **(Fig. 3F)**, characterized by the upregulation of *Tfrc*, *Cdkn1a*, *Il12rb1*, *Ada*, and *Icosl*, and the downregulation of *Gpr183*, *Ccr2*, *Ager*, and *Clcf1*. Notably, the upregulation of *Cdkn1a* (p21) suggests a potential disruption in cell cycle progression despite the activation signals. Consistent with this, the "positive regulation of cytokine production" signature **(Fig. 3G)** displayed a highly skewed profile, with upregulation of *Thbs1*, *Hspd1*, *Lta*, *Il12rb1*, and *Xcl1*, but a significant downregulation of key effector cytokines such as *Ifng* and *Il4*. Furthermore, the "T cell apoptosis" signature **(Fig. 3H)** exhibited a bidirectional dysregulation, characterized by the upregulation of *Lgals3bp*, *Adam8*, *Ada*, and *Zc3h8*, alongside a notable downregulation of pro-apoptotic mediators such as *Bbc3* (PUMA), *Tsc22d3*, and *Efna1*. To further distill the core molecular drivers, we highlighted a subset of critical DEGs (summarized in **Supplementary Table 4**). Specifically, the upregulation of co-stimulatory molecules *Icos* and *Tnfrsf4* (OX40) indicates enhanced activation potential, while the concurrent upregulation of *Cdkn1a* (p21) and *Il12rb1* points to cell cycle arrest and a skewing toward Th1 differentiation. Moreover, the upregulation of *Tnfaip3* (A20) and *Clcf1* suggests an attempt to restrain excessive inflammation. In contrast, the downregulation of *Bbc3* (PUMA) indicates a resistance to intrinsic apoptosis, whereas the decreased expression of *Hspd1* (HSP60) implies impaired mitochondrial protein folding and heightened

cellular stress.

Collectively, these transcriptomic findings suggested that Rsad2 loss drives $CD4^+$ T cells toward a hyperactivated, yet functionally fragile, state characterized by impaired effector cytokine production, disrupted cell cycle progression, and an altered apoptotic threshold. Based on this, we hypothesized that *Rsad2* is essential for maintaining the balance between T cell activation, survival, and differentiation. To test this, we next evaluated the functional consequences of *Rsad2* deficiency on T cell proliferation and apoptosis, as well as its impact on T cell differentiation, memory formation, effector T cell generation, and Th1 polarization.

Viperin deficiency enhances $CD4^+$ T cell activation and proliferation during Mtb infection

We next examined the activation and proliferative capacity of Viperin-deficient $CD4^+$ T cells. At 4 weeks post-infection, the frequency of $CD69^+CD25^+$ $CD4^+$ T cells was significantly increased in $Rsad2^{cko}$ mice compared with $Rsad2^{flox}$ mice **(Fig. 4A, B)**, indicating enhanced activation of Mtb-specific $CD4^+$ T cells *in vivo*. In adoptive transfer experiments, the frequency of $CD4^+CD25^+$ T cells was also higher in the lungs of $Rag1^{-/-}$ mice reconstituted with $Rsad2^{cko}$ $CD4^+$ T cells at 1 week post-infection **(Fig. 4C, D)**. CFSE dilution assays revealed enhanced proliferation of $Rsad2^{cko}$ $CD4^+$ T cells at 72 hrs **(Fig. 4E, F)**. Consistent with this, the frequency of $Ki67^+$ $CD4^+$ T cells was also increased in $Rsad2^{cko}$ mice at 4 weeks post-infection **(Fig. 4G, H)**, further supporting enhanced $CD4^+$ T cell proliferation *in vivo*. Cell cycle analysis revealed a significantly higher proportion of $Rsad2^{cko}$ cells in S phase at 48 hrs **(Fig. 4I, J)** and in G2/M phase at 72 hrs **(Fig. 4I, K)**, with a transiently lower G2/M fraction at 48 hrs, suggesting accelerated S-phase entry followed by a synchronized progression into G2/M at later time points. Together, these results demonstrate that Viperin deficiency enhances $CD4^+$ T cell activation and proliferation during Mtb infection.

Viperin regulates CD4$^+$ memory T cell differentiation and the migratory receptor profile

We assessed memory T cell differentiation in vivo. At 4 weeks post-infection, lungs from *Rsad2^{cko}* mice contained a significantly lower frequency of central memory T cells (Tcm, CD44$^+$CD62L$^+$) and a significantly higher frequency of effector memory T cells (Tem, CD44$^+$CD62L$^-$) within the CD4$^+$ compartment, a pattern not observed in the spleen **(Fig. 5A-C)**. In *Rsad2* global knockout mice (*Rsad2$^{-/-}$*), the frequencies of CD4$^+$ Tcm and Tem in the lungs showed similar changes to those seen in *Rsad2* conditional knockout mice, while no notable differences were found in the spleen **(Fig. 5D-F)**. *In vitro*, under TCR stimulation, a greater proportion of *Rsad2*^{cko} naïve CD4$^+$ T cells differentiated into Tem cells, with a corresponding decrease in Tcm cells **(Fig. 5G-I)**.

To investigate the mechanisms underlying this skewed differentiation, we next evaluated the expression of chemokine receptors critical for T cell trafficking. Viperin deficiency did not affect the expression of the lymph node-homing receptor CCR7 **(Fig. 5J, K)**, which aligns with the observed decrease in Tcm. However, it increased the expression of the inflammatory chemokine receptor CXCR3 on splenic, but not lung, CD4$^+$ T cells **(Fig. 5L, M)**. These findings suggest that Viperin not only regulates memory T cell subset differentiation but also influences their migratory capacity. Together, these data indicate Viperin shifts CD4$^+$ T cell differentiation away from a long-lived memory phenotype and toward a more immediate effector state.

Viperin deficiency potentiates Th1 responses by modulating the JAK-STAT signaling pathway

Th1 responses are critical for defense against Mtb. In vivo, we first evaluated the functional capacity of T cells in the lungs of infected *Rsad2^{cko}* mice. Upon stimulation with PMA/ionomycin or ESAT-6, CD4$^+$ T cells from *Rsad2^{cko}* mice produced

significantly more IFN-γ compared to *Rsad2*^{flox} controls **(Fig. 6A, B)**. Consistent with enhanced Th1 polarization, the proportion of T-bet$^+$ CD4$^+$ T cells was increased in *Rsad2*^{cko} mice at 4 weeks post-infection **(Fig. 6C)**. In agreement with these findings, elevated IFN-γ expression was also observed in the lung tissue of *Rsad2*^{cko} mice **(Fig. 6D)**. Notably, this enhanced Th1 response was specific, as the frequencies of Th2 (IL-4$^+$) and Th17 (IL-17$^+$) cells remained unchanged, as did the frequencies of Treg (Foxp3$^+$) cells (**Supplementary Fig. 2A-C**). To corroborate these findings in a full knockout model, we further analyzed *Rsad2*$^{-/-}$ mice. Under antigen-specific or physiological stimulation, elevated frequencies of IFN-γ-producing CD4$^+$ T cells were observed in both the lungs and spleens of *Rsad2*$^{-/-}$ mice compared with controls (**Fig. 6E, F**).

Mechanistically, Viperin deficiency enhanced the mRNA level of CXCL9, a downstream Th1 signature gene, in the lungs of Mtb-infected mice, whereas STAT1 and STAT4 mRNA levels were unchanged and JAK1 mRNA was decreased (**Fig. 6K**). Notably, despite the reduction in JAK1 mRNA, phosphorylated JAK1 protein was increased under Th1 polarization (**Fig. 6L**), suggesting that Viperin deficiency promotes JAK1 activation at the post-translational level, possibly accompanied by negative feedback on JAK1 transcription. Consistent with this, increased phosphorylation of JAK2, JAK1, and STAT4, along with elevated T-bet expression, was observed under Th1 polarization (**Fig. 6L**; quantification in **Supplementary Fig. 3A-D**). Under Th2 polarization, Viperin deficiency reduced JAK1 and STAT6 phosphorylation and GATA3 expression (**Supplementary Fig. 2D**; quantification in **Supplementary Fig. 3B, E, F**). However, Th2 cell frequencies remained unchanged in Mtb-infected mice (**Supplementary Fig. 2A**), likely because the strong Th1-polarizing environment of Mtb infection limits Th2 cells to a minor population. Together, these data establish that Viperin primarily regulates Th1 commitment via the JAK-STAT4-T-bet axis during Mtb infection.

Viperin deficiency confers a survival advantage to CD4$^+$ T cells via Bbc3

downregulation and enhanced pro-survival signaling

Finally, we investigated whether Viperin deficiency affects $CD4^+$ T cell apoptosis and survival. Since PD-1 restrains T cell survival and activation-induced cell death (AICD) is a major form of activation-induced death, we first examined PD-1 expression. PD-1 was lower on lung $CD4^+$ T cells from infected *Rsad2*^{cko} mice (**Fig. 7A, B**) and on donor cells in adoptive transfer models (**Fig. 7C, D**). To directly test whether this corresponded to reduced cell death, we performed Annexin V/PI staining. Unstimulated *Rsad2*^{cko} naïve T cells showed higher early apoptosis but greater overall viability, whereas after 72 hrs of TCR activation they exhibited significantly reduced early and total apoptosis (**Fig. 7E-G**). Thus, Viperin deficiency protects $CD4^+$ T cells from AICD.

To further assess whether these survival advantages were associated with transcriptional changes *in vivo*, we analyzed $CD4^+$ T cells from Mtb-infected mice. Notably, the pro-apoptotic mediator Bbc3 (PUMA) was significantly downregulated in *Rsad2*^{cko} $CD4^+$ T cells **(Fig. 7H)**, consistent with our transcriptomic findings **(Fig. 3H)**. Additionally, Gadd45a mRNA, a negative regulator of T cell proliferation, was significantly downregulated in *Rsad2*^{cko} $CD4^+$ T cells, whereas AKT and PKC-θ mRNA levels were unchanged **(Fig. 7I)**. These data suggest that Viperin deficiency modulates proliferation-related gene expression *in vivo*, while the unchanged AKT and PKC-θ mRNA levels imply that Viperin regulates these pathways at the post-translational level rather than through transcriptional reprogramming. To test this, we assessed pathway activation after TCR stimulation. At 24 hrs post-TCR activation, *Rsad2*^{cko} $CD4^+$ T cells displayed increased phosphorylation of PI3K, AKT, and the downstream effector p70S6K, indicating enhanced PI3K-AKT-mTOR pathway activity **(Fig. 7J, Supplementary Fig. 4A-C)**. Although total PKC-θ was lower, its phosphorylation state (p-PKC-θ/PKC-θ ratio) and subsequent NF-κB p65 phosphorylation were elevated **(Fig. 7J, Supplementary Fig. 4D, E)**. Together, Viperin deficiency promotes $CD4^+$ T cell survival and proliferation by augmenting

PI3K-AKT-mTOR and PKC-θ-NF-κB signaling after TCR activation, and by downregulating Gadd45a and Bbc3 *in vivo*.

Discussion

Viperin (*Rsad2*) is a broad-spectrum antiviral host factor induced by interferons (IFNs), exerting direct antiviral effects by targeting key aspects of viral replication [9-11]. Beyond its canonical antiviral role, Viperin also regulates antibacterial immunity, although the precise molecular mechanisms remain incompletely understood [12]. Our previous studies demonstrated that Viperin impairs macrophage and dendritic cell responses against Mtb, promoting bacterial survival through disruption of the IRAK1-TRAF6-TAK1 complex and inhibition of IFN-γ production [6-8]. However, these studies used global knockout mice, which cannot establish cell-type-specific causality. Here, using T cell-specific conditional knockout (*Rsad2*^{cko}) and adoptive transfer models, we demonstrate that Viperin acts intrinsically in CD4$^+$ T cells to suppress anti-mycobacterial immunity. Viperin deficiency in CD4$^+$ T cells significantly reduced bacterial burden in the lungs, accompanied by an increased proportion of Mtb-specific CD4$^+$, but not CD8$^+$, T cells. These findings position Viperin as a critical negative regulator of adaptive immunity against Mtb and prompted us to investigate its effects on CD4$^+$ T cell activation, proliferation, differentiation, and apoptosis.

Our transcriptomic analysis revealed that Viperin deficiency drives CD4$^+$ T cells toward a hyperactivated yet functionally fragile state, characterized by enhanced activation and proliferation but dysregulated effector cytokine production and an altered apoptotic threshold. Mechanistically, we identify Viperin as a bidirectional regulator of Th1/Th2 differentiation through the JAK-STAT pathway. Under Th1-polarizing conditions, Viperin deficiency enhances IL-12-induced JAK2/JAK1-STAT4 signaling, upregulates T-bet, and promotes IFN-γ production. Conversely, under Th2-polarizing conditions, Viperin deficiency impairs IL-4-mediated JAK1-STAT6-GATA3 signaling. This bidirectional regulation suggests that Viperin acts as an "intrinsic brake" on Th1 differentiation while simultaneously serving as a "positive regulator" of Th2 differentiation. Consistent with our findings, previous

studies have also implicated Viperin in the regulation of JAK-STAT signaling [7], and its conserved N-terminal domain or SAM enzymatic activity may mediate interactions with specific JAK kinases or receptor complexes [13], thereby differentially interfering with their phosphorylation and activation. Notably, although in vitro Th2 polarization clearly revealed a modulatory effect of Viperin on the JAK1-STAT6-GATA3 axis, Th2 cell frequencies remained unchanged in Mtb-infected mice. This discrepancy likely reflects the strong Th1-polarizing environment of Mtb infection, in which Th2 cells represent only a minor population in the lungs and spleens (Supplementary Fig. 2A-C), and their changes are masked by the dominant Th1 response. Therefore, the in vitro polarization experiments reveal the intrinsic modulatory potential of Viperin on the Th2 pathway, whereas whether this potential manifests in vivo depends on the local cytokine milieu and infection stage. This observation also suggests that Viperin's regulation of $CD4^+$ T cell function is pathogen-specific: during Mtb infection, its dominant role is to restrain Th1 polarization rather than to regulate Th2 responses. This is consistent with the fact that antiviral immunity relies primarily on $CD8^+$ T cell effector function, whereas anti-mycobacterial immunity depends on $CD4^+$ Th1 responses [14-16], further supporting Viperin as a context-dependent regulator of T cell homeostasis rather than a unidirectional immune suppressor or enhancer.

An intriguing question arising from our study is how Viperin's role as a Th1 brake can be reconciled with its well-established antiviral function. This apparent dichotomy may be understood through the lens of IFN-γ biology. IFN-γ is the central cytokine in anti-mycobacterial immunity, essential for macrophage activation, granuloma formation, and bacterial containment, as demonstrated by extensive genetic and clinical evidence—patients with defective IFN-γ signaling are highly susceptible to mycobacterial infections [17, 18]. In viral infections, IFN-γ acts synergistically with type I IFN to amplify antiviral effector programs, and Viperin, as an ISG, reinforces this axis to promote viral clearance[11, 13, 19, 20]. However, in chronic Mtb infection, the role of IFN-γ is more nuanced, while IFN-γ is indispensable

for bacterial control [21], excessive or sustained IFN-γ signaling can drive immunopathology, tissue damage, and T cell exhaustion [22]. Our data show that Viperin deficiency enhances $CD4^+$ Th1 responses and IFN-γ production (Fig. 6), which correlates with improved bacterial control but also with a hyperactivated, metabolically fragile T cell state (Fig. 3).

The causal link between IFN-γ and mycobacterial killing is one of the most firmly established principles in tuberculosis immunology. Decades of genetic, clinical, and experimental evidence demonstrate that IFN-γ is both necessary and sufficient for macrophage activation, phagolysosomal maturation, and bacterial killing: patients with loss-of-function mutations in IFN-γ signaling components (IFNGR1, IFNGR2, STAT1, IL12RB1) are exquisitely susceptible to disseminated mycobacterial infections, and IFN-γ blockade or neutralization in animal models consistently exacerbates Mtb burden [23-25]. Within this framework, Viperin has been shown to inhibit IFN-γ production in macrophages and lung tissue, with IFN-γ neutralizing antibody reversing the enhanced Mtb survival conferred by Viperin, thereby establishing that Viperin promotes Mtb survival through suppression of IFN-γ [7]. Building on this, our study extends the mechanism to the T cell compartment: Viperin-deficient $CD4^+$ T cells produce significantly more IFN-γ under Th1-polarizing conditions (Fig. 6), and this is accompanied by reduced bacterial burden in vivo. Given the established causal role of IFN-γ in Mtb killing, and the capacity of Viperin to suppress IFN-γ, the enhanced IFN-γ output from Viperin-deficient $CD4^+$ T cells offers a direct explanation for the improved bacterial control. We therefore position Viperin as a T-cell-intrinsic upstream regulator of the IFN-γ–bactericidal axis, rather than a parallel or redundant pathway.

This T-cell-intrinsic regulation of IFN-γ by Viperin also provides a unifying framework for its context-dependent functions. Given the bactericidal function of IFN-γ in anti-mycobacterial immunity, and our data demonstrating that Viperin

deficiency significantly enhances the capacity of $CD4^+$ Th1 cells to produce IFN-γ, we speculate that this enhanced IFN-γ production is an important contributing factor to the reduced bacterial burden observed in Viperin-deficient mice. We therefore propose that Viperin functions as a rheostat for IFN-γ signaling: in acute viral infection, it amplifies IFN-γ-mediated antiviral responses; in chronic bacterial infection, it restrains excessive IFN-γ-driven Th1 polarization to prevent immunopathology, while also attenuating IFN-γ-dependent bactericidal capacity, thereby favoring Mtb survival. This model is consistent with the hypothesis that Viperin-mediated $CD4^+$ T cell dysfunction during chronic HIV infection may contribute to latent TB reactivation, as impaired IFN-γ responses are a known risk factor for TB reactivation. A schematic model illustrating the dual role of Viperin in antiviral and antimycobacterial immunity is presented in **Supplementary Fig. 5**.

Our findings also reveal a tissue-specific dissociation between CXCR3 expression and Tem differentiation. In the spleen, CXCR3 was upregulated in *Rsad2*^{cko} $CD4^+$ T cells without a concurrent increase in Tem frequency, whereas in the lungs, Tem skewing occurred independently of CXCR3 changes. CXCR3 is a Th1-associated chemokine receptor that is expressed on a large fraction of effector and memory T cells and plays a major role in recruiting these cells to inflamed tissues [26]. Notably, CXCR3 is also a hallmark of effector memory T cells (Tem), which are characterized by the loss of CCR7 and CD62L and acquisition of rapid effector functions. In Mtb infection, CXCR3-expressing $CD4^+$ T cells are enriched at sites of infection and their frequency inversely correlates with bacterial burden [27]. However, CXCR3 also plays a context-dependent role in shaping T cell fate during chronic infection [28]. We propose that this discrepancy reflects the sequential and spatial dynamics of the T cell response to Mtb infection. The spleen acts as a systemic “priming and launchpad,” where Viperin deficiency confers a “migration license” by upregulating CXCR3. However, the splenic microenvironment is not sufficient to sustain terminal Tem differentiation locally. Consequently, these highly migratory $CXCR3^+$ cells are

mobilized to leave the spleen and traffic to the primary site of infection. In contrast, the Mtb-infected lung provides a potent inflammatory niche enriched in IL-12, IFN-γ, and chemokines (e.g., CXCL9), that drives terminal Tem differentiation. Upon reaching the lungs, CXCR3 may be downregulated in response to local signals to prevent hyper-inflammatory tissue damage and facilitate tissue retention, a phenomenon observed in respiratory infection models where $CXCR3^{hi}$ cells lose CXCR3 and become retained in peribronchial areas [29, 30]. This model aligns with our broader concept of Viperin as a context-dependent regulator of T cell homeostasis and highlights the importance of tissue-specific signals in shaping $CD4^+$ T cell fate.

Finally, we identify Bbc3 (PUMA) and Gadd45a as key downstream effectors through which Viperin regulates the apoptotic threshold and proliferative capacity of $CD4^+$ T cells. Our data demonstrate that Viperin-deficient $CD4^+$ T cells exhibit enhanced activation of both PI3K-Akt-mTOR and PKC-θ-NF-κB pathways upon TCR engagement, concomitant with transcriptional downregulation of Bbc3 and Gadd45a *in vivo*. While these findings are correlative, they point to a testable model; pathway-specific inhibitors or promoter reporter assays will be needed to dissect the precise transcriptional regulation. Mechanistically, the PI3K-Akt pathway can regulate Bbc3 transcription through FOXO transcription factors: when Akt is activated, FOXO is phosphorylated and retained in the cytoplasm, losing transcriptional activity [31]; when PI3K/Akt signaling is inhibited, FOXO enters the nucleus and binds to the Bbc3 promoter to initiate its transcription [32]. In addition, PI3K/AKT signaling cooperates with Myc to suppress FOXO3a-dependent PUMA and GADD45a gene expression, with Myc being rapidly recruited to PUMA and GADD45a chromatin to induce inhibitory histone modifications [33]. Consistent with this, mTOR inhibition by torin significantly upregulates Bbc3 expression, suggesting that mTOR signaling helps maintain Bbc3 in a low-expression state [34]. These mechanistic links suggest that Viperin deficiency, by activating PI3K-Akt-mTOR signaling, downregulates Bbc3 and

Gadd45a through FOXO inactivation and Myc-mediated transcriptional repression, thereby elevating the apoptotic threshold and enhancing proliferative capacity. This concurrent downregulation of the pro-apoptotic mediator Bbc3 and the proliferation brake Gadd45a, coupled with enhanced pro-survival signaling, offers a coherent explanation for the numerical advantage of antigen-specific $CD4^+$ T cells observed in Viperin-deficient models.

In summary, Viperin acts as a central hub for maintaining $CD4^+$ T cell homeostasis by coordinately regulating Th1 differentiation, proliferation, and apoptosis. This dual role—restraining excessive Th1 polarization while setting the apoptotic and proliferative threshold—positions Viperin as a rheostat that tunes the intensity and durability of $CD4^+$ T cell responses. Therapeutically, transiently blocking Viperin in T cells may offer a synergistic host-directed strategy against tuberculosis by enhancing Th1 function, expanding the T cell pool, and prolonging T cell survival.

References

1. Trajman A, et al., *Tuberculosis.* Lancet, 2025. **405**(10481): p. 850-866.
2. Dheda K, Barry CE, 3rd, and Maartens G, *Tuberculosis.* Lancet, 2016. **387**(10024): p. 1211-26.
3. Roy Chowdhury R, et al., *A multi-cohort study of the immune factors associated with M. tuberculosis infection outcomes.* Nature, 2018. **560**(7720): p. 644-648.
4. Bromley JD, et al., *CD4(+) T cells re-wire granuloma cellularity and regulatory networks to promote immunomodulation following Mtb reinfection.* Immunity, 2024. **57**(10): p. 2380-2398 e6.
5. Chen S, et al., *Crucial Roles of RSAD2/viperin in Immunomodulation, Mitochondrial Metabolism and Autoimmune Diseases.* Inflammation, 2025. **48**(2): p. 520-540.
6. Zhou X, et al., *Viperin impairs the innate immune response through the IRAK1-TRAF6-TAK1 axis to promote Mtb infection.* Sci Signal, 2022. **15**(754): p.

783 eabe1621.
784 7. Liang Y, et al., *Viperin inhibits interferon-gamma production to promote*
785 *Mycobacterium tuberculosis survival by disrupting TBK1-IKKepsilon-IRF3-axis and*
786 *JAK-STAT signaling.* Inflamm Res, 2024. **73**(6): p. 897-913.
787 8. Zhou X, et al., *Viperin deficiency promotes dendritic cell activation and function*
788 *via NF-kappaB activation during Mycobacterium tuberculosis infection.* Inflamm
789 Res, 2023. **72**(1): p. 27-41.
790 9. Rivera-Serrano EE, et al., *Viperin Reveals Its True Function.* Annu Rev Virol, 2020.
791 **7**(1): p. 421-446.
792 10. Hinson ER and Cresswell P, *The antiviral protein, viperin, localizes to lipid droplets*
793 *via its N-terminal amphipathic alpha-helix.* Proc Natl Acad Sci U S A, 2009.
794 **106**(48): p. 20452-7.
795 11. Teng TS, et al., *Viperin restricts chikungunya virus replication and pathology.* J
796 Clin Invest, 2012. **122**(12): p. 4447-60.
797 12. Helbig KJ, et al., *The interferon stimulated gene viperin, restricts Shigella. flexneri*
798 *in vitro.* Sci Rep, 2019. **9**(1): p. 15598.
799 13. Kahler NL, et al., *ISG15-USP18 signaling restrains viperin-dependent metabolic*
800 *antiviral restriction.* bioRxiv, 2026.
801 14. Mattingly CLR, et al., *Human lung CD8(+) tissue-resident memory T cell-derived*
802 *interferon-gamma orchestrates subset-specific antiviral programming in airway*
803 *epithelial cells.* Immunity, 2025. **58**(12): p. 3006-3023 e5.
804 15. Robinson RT, Orme IM, and Cooper AM, *The onset of adaptive immunity in the*
805 *mouse model of tuberculosis and the factors that compromise its expression.*
806 Immunol Rev, 2015. **264**(1): p. 46-59.
807 16. Prezzemolo T, et al., *Functional Signatures of Human CD4 and CD8 T Cell*
808 *Responses to Mycobacterium tuberculosis.* Front Immunol, 2014. **5**: p. 180.
809 17. Dow CT and Obaid L, *Proposing Bromo-Epi-Androsterone for Host-Directed*
810 *Therapy Against Tuberculosis.* Pathogens, 2025. **14**(11).

18. Imran M, et al., *IFN-gamma-Driven macrophage responses in the immunity to Mycobacterium tuberculosis and Mycobacterium leprae.* Front Cell Infect Microbiol, 2025. **15**: p. 1679691.
19. Sanda C, et al., *Differential gene induction by type I and type II interferons and their combination.* J Interferon Cytokine Res, 2006. **26**(7): p. 462-72.
20. Giugliano S, et al., *Hepatitis C virus infection induces autocrine interferon signaling by human liver endothelial cells and release of exosomes, which inhibits viral replication.* Gastroenterology, 2015. **148**(2): p. 392-402 e13.
21. Sakai S, et al., *CD4 T Cell-Derived IFN-gamma Plays a Minimal Role in Control of Pulmonary Mycobacterium tuberculosis Infection and Must Be Actively Repressed by PD-1 to Prevent Lethal Disease.* PLoS Pathog, 2016. **12**(5): p. e1005667.
22. Mackerness KJ, et al., *Pronounced virus-dependent activation drives exhaustion but sustains IFN-gamma transcript levels.* J Immunol, 2010. **185**(6): p. 3643-51.
23. Jouanguy E, et al., *A human IFNGR1 small deletion hotspot associated with dominant susceptibility to mycobacterial infection.* Nat Genet, 1999. **21**(4): p. 370-8.
24. Tsumura M, et al., *Dominant-negative STAT1 SH2 domain mutations in unrelated patients with Mendelian susceptibility to mycobacterial disease.* Hum Mutat, 2012. **33**(9): p. 1377-87.
25. Gemici Karaaslan B, et al., *Interferon Gamma in Sickness Predisposing to Mycobacterial Infectious Diseases.* Balkan Med J, 2024. **41**(5): p. 326-332.
26. Rubinstein A, et al., *CXCR3-Expressing T Cells in Infections and Autoimmunity.* Front Biosci (Landmark Ed), 2024. **29**(8): p. 301.
27. Shanmugasundaram U, et al., *Pulmonary Mycobacterium tuberculosis control associates with CXCR3- and CCR6-expressing antigen-specific Th1 and Th17 cell recruitment.* JCI Insight, 2020. **5**(14).
28. Chakravarty SD, et al., *The chemokine receptor CXCR3 attenuates the control of*

chronic Mycobacterium tuberculosis infection in BALB/c mice. J Immunol, 2007. **178**(3): p. 1723-35.

29. Abboud G, et al., *Tissue-specific programming of memory CD8 T cell subsets impacts protection against lethal respiratory virus infection.* J Exp Med, 2016. **213**(13): p. 2897-2911.
30. Kohlmeier JE, et al., *Inflammatory chemokine receptors regulate CD8(+) T cell contraction and memory generation following infection.* J Exp Med, 2011. **208**(8): p. 1621-34.
31. You H, et al., *FOXO3a-dependent regulation of Puma in response to cytokine/growth factor withdrawal.* J Exp Med, 2006. **203**(7): p. 1657-63.
32. Fitzwalter BE, et al., *Autophagy Inhibition Mediates Apoptosis Sensitization in Cancer Therapy by Relieving FOXO3a Turnover.* Dev Cell, 2018. **44**(5): p. 555-565 e3.
33. Amente S, et al., *Myc and PI3K/AKT signaling cooperatively repress FOXO3a-dependent PUMA and GADD45a gene expression.* Nucleic Acids Res, 2011. **39**(22): p. 9498-507.
34. Park S, Sim H, and Lee K, *Rapamycin-resistant and torin-sensitive mTOR signaling promotes the survival and proliferation of leukemic cells.* BMB Rep, 2016. **49**(1): p. 63-8.

Statements

Acknowledgements

The authors acknowledge the support of Professor Zhinan Yin and his team at Jinan University, who generously provided the tool mice essential for the pilot studies of this work.

Statement of Ethics

This study protocol was reviewed and approved by Ethics Committee of the Southern Medical University, approval number [202501].

Conflict of Interest Statement

The authors have no conflicts of interest to declare.

Funding Sources

This work was supported by Major Project of Guangzhou National Laboratory (GZNL2024A01023), Prevention and Control of Emerging and Major Infectious Diseases-National Science and Technology Major Project (2025ZD01907200), National Natural Science Foundation of China (82272344, 82472303, 82470013), Guangdong Basic and Applied Basic Research Foundation (2024A1515013089, 2024A1515011320， 2025A1515012373), Provincial Key Laboratory of Immune Regulation and Immunotherapy (2022B1212010009).

Author Contributions

Xinying Zhou: contributed to study concept and design, drafting of the manuscript, study supervision, obtained funding and critical revision of the manuscript. All authors read and approved the final manuscript. **Yun Liang**: acquisition of data, analysis and interpretation of data, drafting of the manuscript, statistical analysis and critical revision of the manuscript. **Lingming Lin, Hongxuan Li**: acquisition of data, analysis and interpretation of data, drafting of the manuscript, **Huilan Niu, Zhenyu Han and Minna Xu**: contributed to acquisition of data. **Qian Wen, Chaoying Zhou,**

and Liang Zhou: contributed to study concept; **Li Ma**: contributed to study concept and design, study supervision, obtained funding and critical revision of the manuscript.

Data Availability Statement

The raw data supporting the conclusions of this article will be made available by the authors, without undue reservation.

Figure

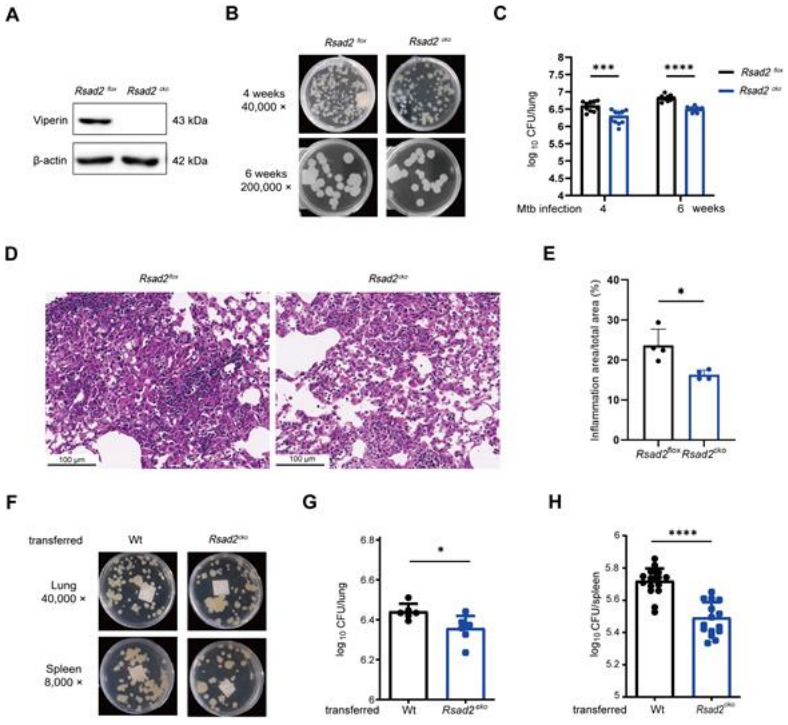


Fig. 1 Viperin deficiency in CD4⁺ T cells confers enhanced resistance to Mtb infection.

(A). Naïve CD4⁺ T cells were isolated from 8-week-old *Rsad2*^{cko} and *Rsad2*^{flox} mouse splenocytes using magnetic beads. *Rsad2* mRNA and Viperin protein levels in cell lysates were detected western blot. Data are representative of three independent experiments.

(B-C). *Rsad2*^{cko} and *Rsad2*^{flox} mice were infected via aerosol with Mtb H37Rv using a standardized Glas-Col inhalation exposure system. Briefly, 1 × 10^6 CFU of Mtb suspended in 3 mL PBS was loaded into the nebulizer, and six mice were placed in the circular chamber and exposed simultaneously for 30 min. Animals were sacrificed at 4 and 6 weeks post-infection. Bacterial CFU **(C)** and log_{10} CFU **(D)** in the lungs of individual mice are shown (n = 5-6 per group at each time point). Under our calibrated conditions, the implanted lung dose at Day 1 was approximately 10,000 CFU per mouse.

(D). Hematoxylin-eosin-stained paraffin sections of lungs from *Rsad2*^{cko} and *Rsad2*^{flox} mice at 6 weeks post-infection with Mtb (scale bar: 100 μm).

(E). Quantification of the inflammatory area in lung tissues. The inflammatory area and total lung tissue area were measured using Fiji software (ImageJ) via the Color Threshold method (HSB color space) under fixed threshold parameters, followed by binarization. The inflammatory area percentage was calculated as (inflammatory area/total lung tissue area) × 100%.

(F-H). *Rag1*$^{-/-}$ mice were intravenously administered either *Rsad2*^{flox} (n = 5) or *Rsad2*^{cko} (n = 6) CD4^{+} T cells. CFU **(F)** and log_{10} CFU in lungs **(G)** and spleens **(H)** are shown.

Statistical significance was determined using unpaired Student's t-test (E, G, H) or two-way ANOVA followed by Sidak's multiple-comparison test (C). Data are presented as mean ± SEM; For CFU analysis, log_{10}-transformed values were used for statistical comparisons. ns = not significant, *P ≤ 0.05, ****P ≤ 0.0001.

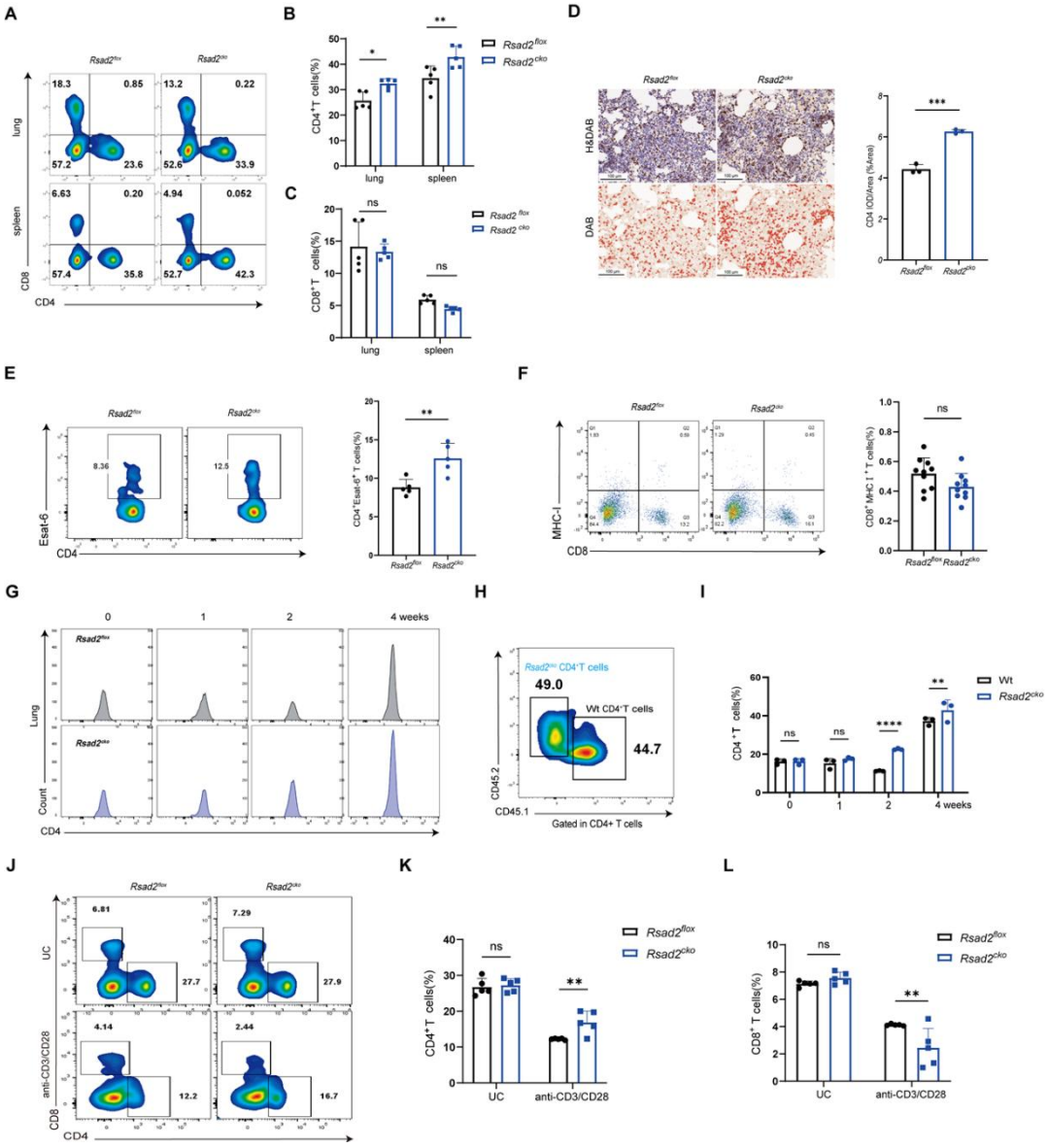


Fig. 2 Viperin deficiency intrinsically enhances Mtb-specific CD4⁺ T cell accumulation and early activation without affecting CD8⁺ T cell responses.

(A) Flow cytometry histogram of CD4 and CD8a expression in lung and spleen T cells from *Rsad2*^{flox} and *Rsad2*^{cko} mice 4 weeks post-infection.

(B-C) Frequencies of CD4⁺ T cells (B) and CD8⁺ T cells (C) in lungs and spleens of *Rsad2*^{flox} (n=5) and *Rsad2*^{cko} (n=5) mice 4 weeks after *Mtb* infection.

(D) Immunohistochemical detection of CD4⁺ T cells in lung sections from *Rsad2*^{flox} and *Rsad2*^{cko} mice 4 weeks after infection. Top: H&E with DAB, nuclei in blue; bottom: DAB staining for CD4, red signal indicates CD4⁺ T cells (scale bar = 100 μm). Right panel shows quantification of CD4⁺ T cells as IOD/Area.

(E) Flow cytometry histogram of ESAT-6_{1-20} tetramer$^+$ CD4$^+$ T cells in lungs of *Rsad2^{flox}* and *Rsad2^{cko}* mice 4 weeks post-infection. Frequencies of ESAT-6$^+$ CD4$^+$ T cells are shown (*Rsad2^{flox}* n=4, *Rsad2^{cko}* n=4).

(F) Representative flow cytometry plots and quantification of Mtb-specific tetramer$^+$ CD8$^+$ T cells in the lungs of Rsad2flox and Rsad2cko mice at 4 weeks post-infection.

(G) Representative histograms of CD45.2$^+$ *Rsad2^{cko}* and CD45.1$^+$ Wt CD4$^+$ T cells in *Rag1$^{-/-}$* mice at 0, 1, 2, and 4 weeks after *Mtb* infection.

(H) Flow cytometry histogram of *Rag1$^{-/-}$* mice co-transferred with CD45.2$^+$ *Rsad2*^{cko} and CD45.1$^+$ Wt CD4$^+$ T cells, analyzed 4 weeks after *Mtb* infection.

(I) Frequencies of transferred CD4$^+$ T cells in *Rag1$^{-/-}$* mice at 0, 1, 2, and 4 weeks after infection.

(J) Representative flow cytometry plots showing CD4 and CD8 staining in spleen T cells of *Rsad2*^{flox} and *Rsad2*^{cko} mice under unstimulated 0 h (UC) and anti-CD3/CD28 24 hrs (anti-CD3/CD28) conditions.

(K) Frequency of CD4$^+$T cells in spleen T cells of *Rsad2*^{flox} and *Rsad2^{cko}* mice under unstimulated 0 h (UC) and anti-CD3/CD28 24 hrs (anti-CD3/CD28) conditions.

(L) Frequency of CD8$^+$T cells in spleen T cells of *Rsad2^{flox}* and *Rsad2^{cko}* mice under unstimulated 0 h (UC) and anti CD3/CD28 24 hrs (anti-CD3/CD28) conditions.

Statistical significance was determined using unpaired Student's t-test (B-F) or two-way ANOVA followed by Sidak's multiple-comparison test (I, K, L). Data are presented as mean ± SEM; ns = not significant, *P ≤ 0.05, **P ≤ 0.01, ***P ≤ 0.001, ****P ≤ 0.0001. Data are representative of three independent experiments.

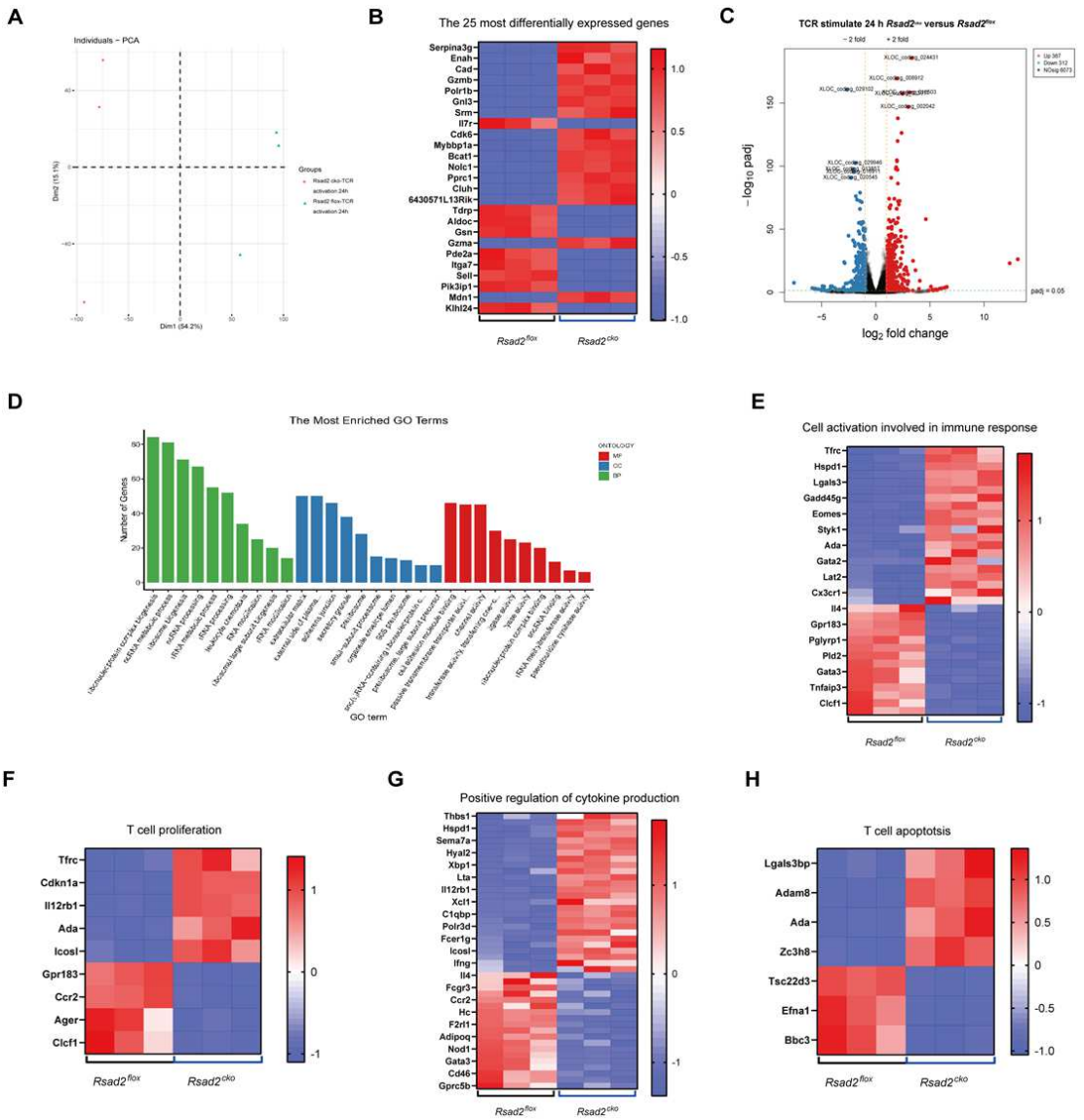


Fig. 3 Transcriptional profiling reveals Viperin orchestrates CD4⁺ T cell fate by regulating survival, activation, and effector programs.

(A) PCA of *Rsad2*^{cko} and *Rsad2*^{flox} CD4⁺ T cells 24 hrs after TCR stimulation, based on normalized gene counts after low-expression filtering. PCA confirmed a clear separation between the two groups.

(B) Volcano plot showing differentially expressed genes (DEGs) in *Rsad2*^{cko} versus *Rsad2*^{flox} CD4⁺ T cells 24 hrs after TCR stimulation. Significantly upregulated and downregulated genes are colored red and light blue, respectively. A total of 699 DEGs were identified.

(C) Heatmap showing the 25 most differentially expressed genes in *Rsad2*^{cko} and

Rsad2^{flox} CD4^{+} T cells after 24 hrs of TCR stimulation. The heatmap reveals profound downregulation of effector molecules (Gzma, Gzmb) and survival/proliferation regulators (Il7r, Cdk6) in Rsad2cko cells.

(D) GO enrichment analysis of DEGs in *Rsad2*^{cko} versus *Rsad2*^{flox} CD4^{+} T cells 24 hrs after TCR stimulation. Enriched pathways were predominantly associated with RNA metabolism, ribosome biogenesis, and translational machinery.

(E–H) Heatmaps showing selected genes from the enriched pathways identified in (D). Four functional categories were selected because they represent core processes governing CD4^{+} T cell protective immunity against Mtb, spanning activation, effector function, proliferation, and survival: **(E)** immune response activation, **(F)** T cell proliferation, **(G)** cytokine production, and **(H)** apoptosis. Detailed gene lists and expression changes are provided in **Supplementary Table 4**.

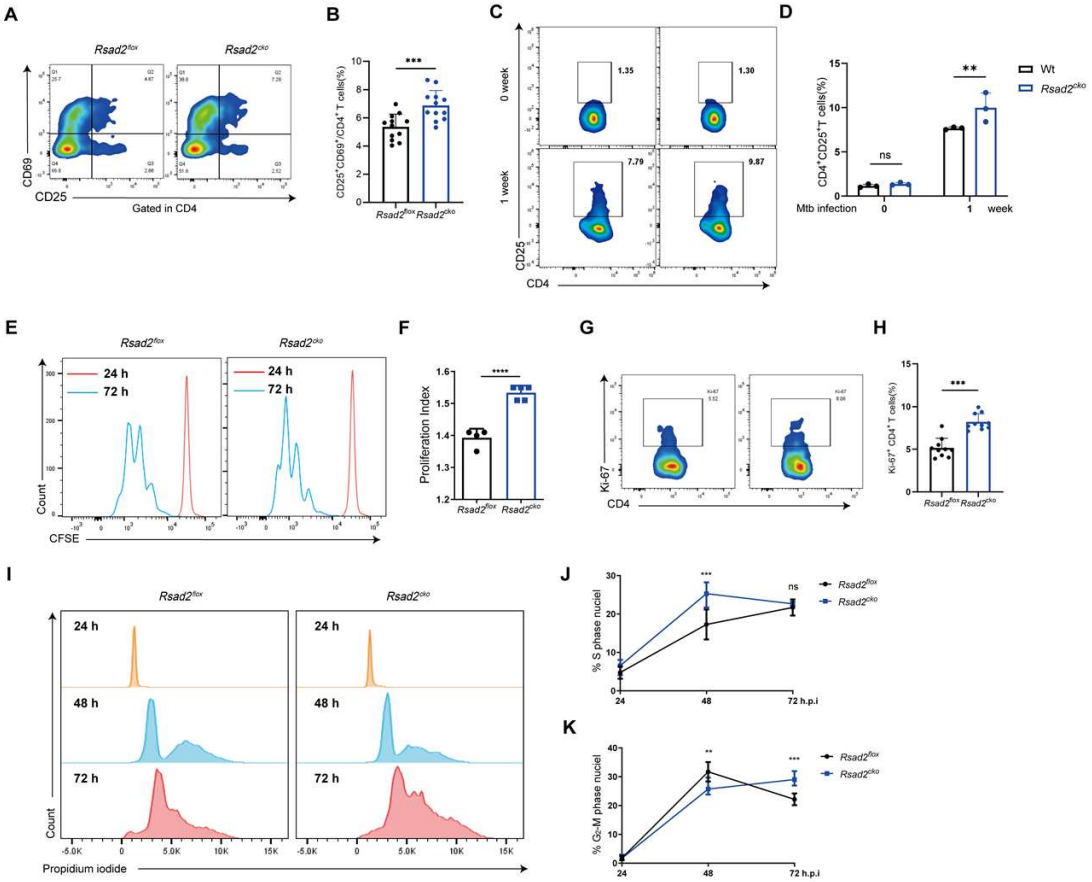


Fig. 4 Viperin deficiency enhances CD4$^+$ T cell activation and proliferation during Mtb infection.

(A-B) Representative flow cytometry density plots **(A)** and frequencies **(B)** of CD69$^+$CD25$^+$ CD4$^+$ T cells in *Rsad2^{cko}* and *Rsad2^{flox}* mice at 4 weeks post-Mtb infection.

(C–D) Representative flow cytometry density plots **(C)** and frequencies **(D)** of CD4$^+$CD25$^+$ T cells in the lungs of Rag1^{-}/$^{-}$ mice reconstituted with Rsad2flox or Rsad2cko CD4$^+$ T cells at 1 week post-Mtb infection.

(E) Representative CFSE dilution histograms **(E)** and proliferation index **(F)** of *Rsad2^{cko}* and *Rsad2^{flox}* CD4$^+$ T cells at 72 hrs after anti-CD3/CD28 stimulation.

(G–H) Representative flow cytometry plots **(G)** and frequencies **(H)** of Ki67$^+$ CD4$^+$ T cells in *Rsad2^{cko}* and *Rsad2^{flox}* mice at 4 weeks post-Mtb infection.

(I-K) Representative propidium iodide (PI) staining histograms of *Rsad2^{cko}* and *Rsad2^{flox}* CD4$^+$ T cells at 24, 48, and 72 hrs after anti-CD3/CD28 stimulation.

Statistical significance was determined using unpaired Student's t-test (A-B, E-F, G-H) or two-way ANOVA followed by Sidak's multiple-comparison test (C-D, I-K). Data are presented as mean ± SEM; ns = not significant, *P ≤ 0.05, **P ≤ 0.01, ***P ≤ 0.001, ****P ≤ 0.0001. Data are representative of three independent experiments.

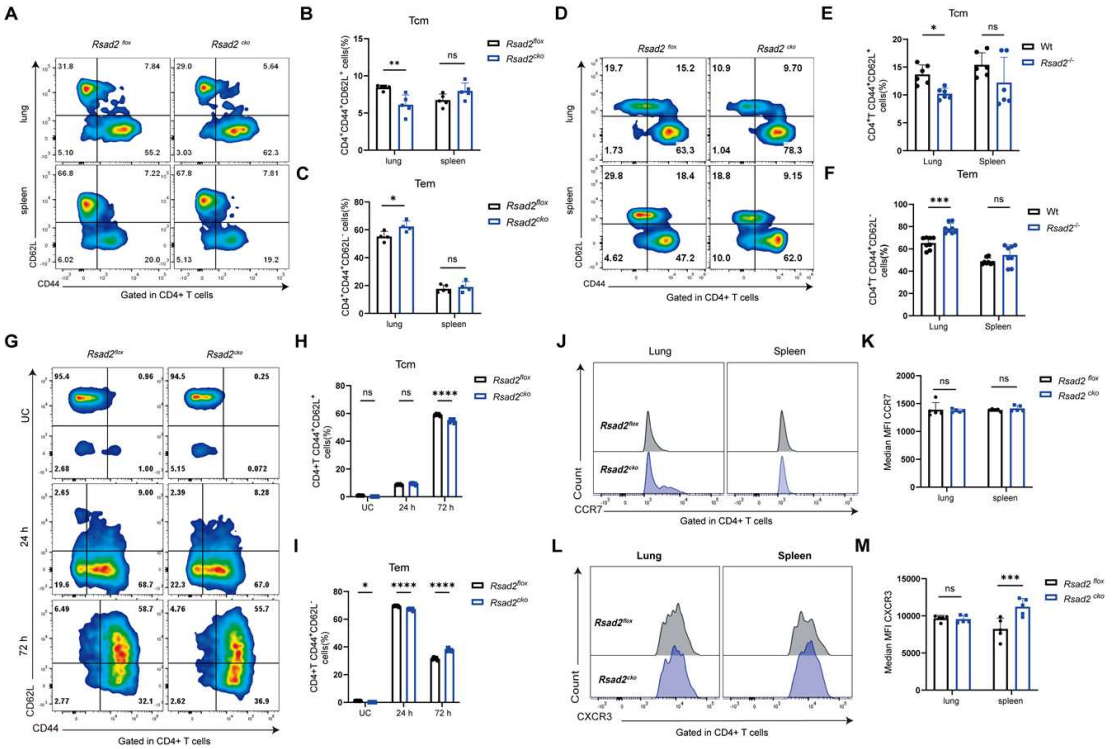


Fig. 5 Viperin deficiency skews CD4⁺ T cell differentiation toward an effector memory phenotype and alters CXCR3 expression

(A) Representative density plots of Tcm ($CD44^+CD62L^+$) and Tem ($CD44^+CD62L^-$) within the $CD4^+$ compartment in the lungs (top) and spleens (bottom) of *Rsad2*^{flox} and *Rsad2*^{cko} mice at 4 weeks post-infection with *Mtb*. **(B, C)** Quantification of the frequencies of $CD4^+$ Tcm **(B)** and $CD4^+$ Tem **(C)** cells in the lungs and spleens of *Rsad2*^{flox} and *Rsad2*^{cko} mice at 4 weeks post-infection.

(D-F) Representative density plots **(D)** and quantification of $CD4^+$ Tcm **(E)** and $CD4^+$ Tem. **(F)** frequencies in the lungs and spleens of Wt and *Rsad2*$^{-/-}$ mice at 4 weeks post-*Mtb* infection.

(G-I) Representative density plots **(G)** and quantification of Tcm **(H)** and Tem **(I)** frequencies among *Rsad2*^{flox} and *Rsad2*^{cko} $CD4^+$ T cells after 0, 24, and 72 hrs of anti-CD3/CD28 stimulation in vitro.

(J, K) Representative histograms **(J)** and quantification of mean fluorescence intensity (MFI) **(K)** of CCR7 expression on $CD4^+$ T cells from the lungs of *Rsad2*^{flox} and *Rsad2*^{cko} mice at 4 weeks post-infection.

(L, M) Representative histograms **(L)** and quantification of MFI **(M)** of CXCR3 expression on $CD4^+$ T cells from the spleens of *Rsad2*^{flox} and *Rsad2*^{cko} mice at 4 weeks post-infection.

Statistical significance was determined by two-way ANOVA followed by Sidak's multiple-comparison test (B, C, E, F, H, I) or unpaired two-tailed Student's t test (K, M). Data are presented as mean ± SEM; ns = not significant, *P ≤ 0.05, **P ≤ 0.01, ***P ≤ 0.001, ****P ≤ 0.0001. Data are representative of three independent experiments.

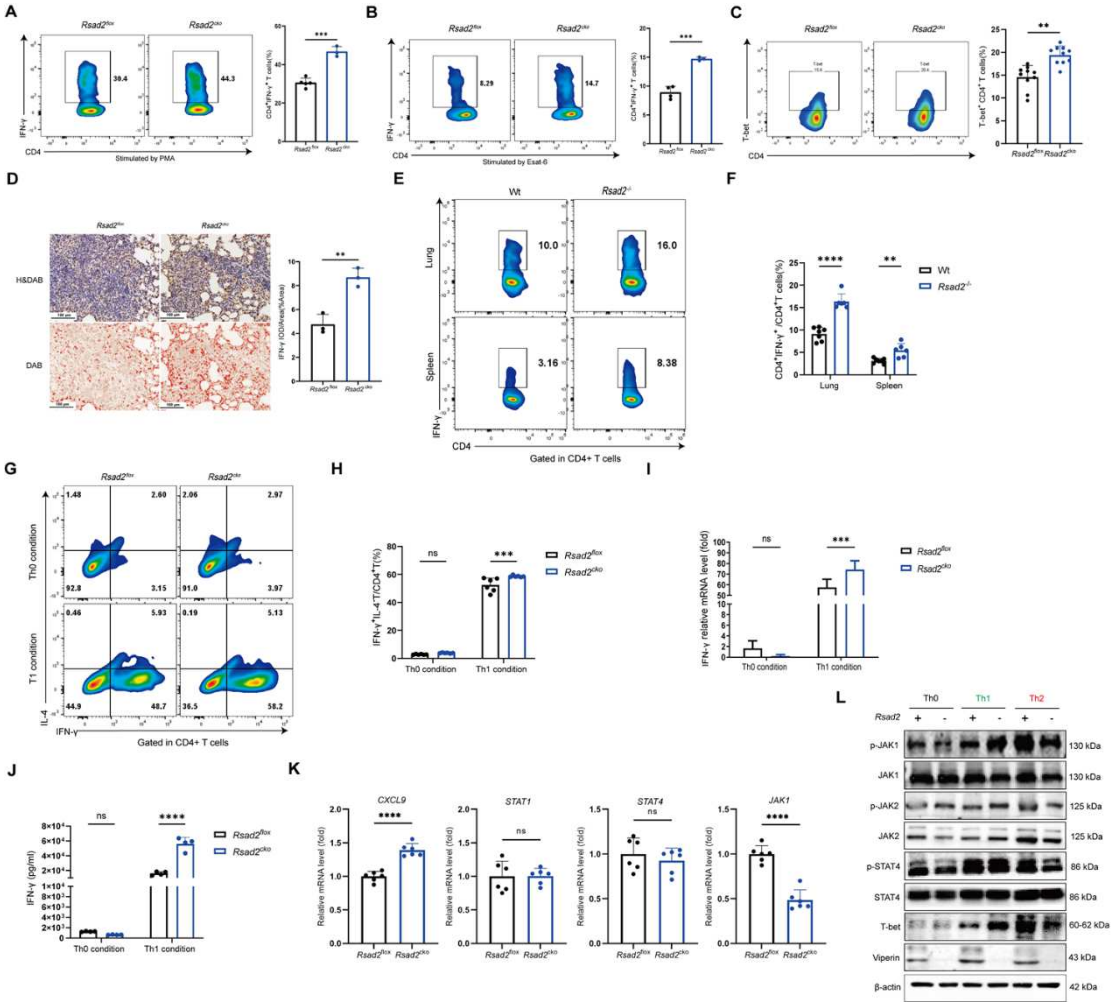


Fig. 6 Viperin deficiency potentiates Th1 responses by modulating the JAK-STAT signaling pathway.

(A) Representative flow cytometry plots and frequencies of $CD4^+IFN\text{-}\gamma^+$ T cells in the lungs of *Rsad2*^{flox} (n=4) and *Rsad2*^{cko} (n=4) mice at 4 weeks post-Mtb infection after stimulation with PMA/ionomycin for 5 hrs.

(B) Representative flow cytometry plots and frequencies of $CD4^+IFN\text{-}\gamma^+$ T cells in the

lungs of *Rsad2*^{flox} (n=4) and *Rsad2*^{cko} (n=4) mice at 4 weeks post-Mtb infection after stimulation with ESAT-6_{1-20} peptide for 5 hrs.

(C) Representative flow cytometry plots and frequencies of T-bet^{+} CD4^{+} T cells in the lungs of *Rsad2*^{flox} (n=5) and *Rsad2*^{cko} (n=5) mice at 4 weeks post-Mtb infection.

(D) IFN-γ antibody staining of lung tissue sections from *Rsad2*^{flox} (n=3) and *Rsad2*^{cko} (n=3) mice 4 weeks after Mtb infection (Top: H&E with DAB, blue indicates the cell nucleus; bottom: DAB immunohistochemical staining of IFN-γ protein, red signal represents IFN-γ^{+} cells) (scale bar = 100 μm), with statistical analysis of IOD/Area (integral optical density/area).

(E, F) Representative flow cytometry plots (E) and frequencies (F) of IFN-γ-producing CD4^{+} T cells in the lungs and spleens of Wt (n=5) and *Rsad2*$^{-/-}$ (n=5) mice at 4 weeks post-Mtb infection after antigen-specific or physiological stimulation.

(G, H) Representative flow cytometry plots **(G)** and frequencies **(H)** of $CD4^+IFN\text{-}\gamma^+IL\text{-}4^-$ T cells from *Rsad2*^{flox} and *Rsad2*^{cko} $CD4^+$ T cells under Th0 or Th1 polarization conditions.

(I) Relative mRNA level of IFN-γ in *Rsad2*^{flox} and *Rsad2*^{cko} $CD4^+$ T cells under Th0 or Th1 polarization conditions.

(J) IFN-γ content in the culture supernatants of *Rsad2*^{flox} and *Rsad2*^{cko} $CD4^+$ T cells under Th0 or Th1 polarization conditions, detected by ELISA assay.

(K) Relative mRNA levels of CXCL9, STAT1, STAT4, and JAK1 in the lungs of Mtb-infected *Rsad2*^{flox} (n=5) and *Rsad2*^{cko} (n=5) mice.

(L) Representative Western blots of phosphorylated and total JAK1, JAK2, STAT4, T-bet, Viperin, and β-actin in *Rsad2*^{flox} and *Rsad2*^{cko} $CD4^+$ T cells under Th0, Th1, and Th2 polarization conditions.

Statistical significance was determined using unpaired Student's t-test (A-D, F-K) or two-way ANOVA followed by Sidak's multiple-comparison test (H-J). Data are presented as mean ± SEM; ns = not significant, *P ≤ 0.05, **P ≤ 0.01, ***P ≤ 0.001, ****P ≤ 0.0001. Data are representative of at least three independent experiments.

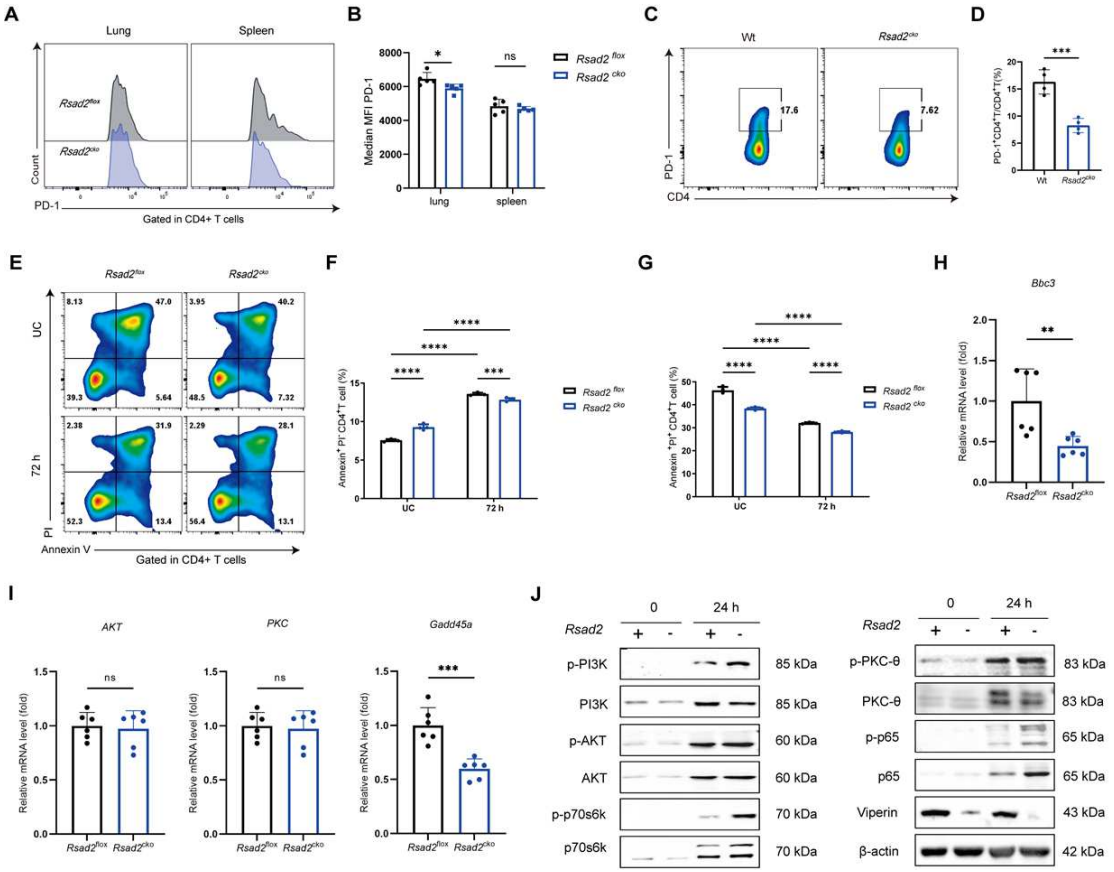


Fig. 7 Viperin deficiency enhances CD4⁺ T cell survival by reducing activation-induced cell death and enhancing pro-survival signaling pathways.

(A) Representative flow cytometry histograms of PD-1 expression on lung and spleen CD4⁺ T cells from *Rsad2*^{flox} and *Rsad2*^{cko} mice 4 weeks after Mtb infection.

(B) Median MFI of PD-1 on lung and spleen CD4⁺ T cells from *Rsad2*^{flox} (n=5) and *Rsad2*^{cko} (n=5) mice 4 weeks after Mtb infection.

(C) Representative flow cytometry plots of CD4⁺PD-1⁺ T cells in the lungs of Rag1$^{-/-}$mice transferred with CD45.1-labeled Wt and CD45.2-labeled *Rsad2*^{cko} CD4⁺ T cells at 1 week after Mtb infection.

(D) Frequencies of CD4⁺PD-1⁺ T cells in the lungs of Rag1$^{-/-}$ mice transferred with CD45.1-labeled Wt (n=4) and CD45.2-labeled *Rsad2*^{cko} (n=4) CD4⁺ T cells at 1 week after Mtb infection.

(E) Representative density plots of apoptotic cells among *Rsad2*^{flox} and *Rsad2*^{cko} CD4⁺ T cells after 72 hrs of unstimulated (UC) or anti-CD3/CD28 stimulation.

(F) Frequencies of early apoptotic (Annexin V⁺PI⁻, top) and late apoptotic (Annexin

V^+PI^+, bottom) cells among *Rsad2*^{flox} and *Rsad2*^{cko} $CD4^+$ T cells after 72 hrs of unstimulated (UC) or anti-CD3/CD28 stimulation.

(G) Frequencies of total apoptotic (Annexin V^+PI^+) $CD4^+$ T cells among *Rsad2*^{flox} and *Rsad2*^{cko} $CD4^+$ T cells after 72 hrs of unstimulated (UC) or anti-CD3/CD28 stimulation.

(H) Relative mRNA level of Bbc3 in $CD4^+$ T cells from the lungs of Mtb-infected *Rsad2*^{flox} (n=5) and *Rsad2*^{cko} (n=5) mice for 4 weeks.

(I) Relative mRNA levels of AKT, PKC-θ, and Gadd45a in $CD4^+$ T cells from the lungs of Mtb-infected *Rsad2*^{flox} (n=5) and *Rsad2*^{cko} (n=5) mice for 4 weeks.

(J) Representative Western blots of phosphorylated and total PI3K, AKT, p70S6K, PKC-θ, NF-κB p65, Viperin, and β-actin in *Rsad2*^{flox} and *Rsad2*^{cko} $CD4^+$ T cells at 0 and 24 hrs after TCR stimulation.

Statistical significance was determined using unpaired Student's t-test (B, D, H, I) or two-way ANOVA followed by Sidak's multiple-comparison test (F, G). Data are presented as mean ± SEM; ns = not significant, *P ≤ 0.05, **P ≤ 0.01, ***P ≤ 0.001, ****P ≤ 0.0001. Data are representative of at least three independent experiments.

Supplementary Files

This is a list of supplementary files associated with this preprint. Click to download.

- SupplementaryMaterial.docx